

UCLA

UCLA Previously Published Works

Title

Atomic structures of fibrillar segments of hIAPP suggest tightly mated β -sheets are important for cytotoxicity.

Permalink

<https://escholarship.org/uc/item/0qf6t1ks>

Authors

Krotee, Pascal
Rodriguez, Jose A
Sawaya, Michael R
et al.

Publication Date

2017

DOI

10.7554/elife.19273

Peer reviewed

Atomic structures of fibrillar segments of hIAPP suggest tightly mated β -sheets are important for cytotoxicity

Pascal Krotee^{1,2,3,4*}, Jose A Rodriguez^{1,2,4}, Michael R Sawaya^{1,2,4}, Duilio Cascio^{1,2,4}, Francis E Reyes⁵, Dan Shi⁵, Johan Hattne⁵, Brent L Nannenga⁵, Marie E Oskarsson⁶, Stephan Philipp⁷, Sarah Griner^{1,2,4}, Lin Jiang^{3,8,9}, Charles G Glabe^{7,10}, Gunilla T Westermark⁶, Tamir Gonen⁵, David S Eisenberg^{1,2,3,4*}

¹Department of Biological Chemistry, Howard Hughes Medical Institute, University of California, Los Angeles, Los Angeles, United States; ²Department of Chemistry and Biochemistry, University of California, Los Angeles, Los Angeles, United States; ³Molecular Biology Institute, University of California, Los Angeles, Los Angeles, United States; ⁴UCLA-DOE Institute, University of California, Los Angeles, Los Angeles, United States; ⁵Janelia Research Campus, Howard Hughes Medical Institute, Ashburn, United States; ⁶Department of Medical Cell Biology, Uppsala University, Uppsala, Sweden; ⁷Department of Molecular Biology and Biochemistry, University of California, Irvine, Irvine, United States; ⁸Department of Neurology, David Geffen School of Medicine, University of California, Los Angeles, Los Angeles, United States; ⁹Brain Research Institute (BRI), University of California, Los Angeles, Los Angeles, United States; ¹⁰Biochemistry Department, Faculty of Science and Experimental Biochemistry Unit, King Fahd Medical Research Center, King Abdulaziz University, Jeddah, Saudi Arabia

*For correspondence: pkrotee@ucla.edu (PK); david@mbi.ucla.edu (DSE)

Competing interests: The authors declare that no competing interests exist.

Funding: See page 20

Received: 30 June 2016

Accepted: 01 December 2016

Published: 03 January 2017

Reviewing editor: Nir Ben-Tal, Tel Aviv University, Israel

© Copyright Krotee et al. This article is distributed under the terms of the [Creative Commons Attribution License](https://creativecommons.org/licenses/by/4.0/), which permits unrestricted use and redistribution provided that the original author and source are credited.

Abstract hIAPP fibrils are associated with Type-II Diabetes, but the link of hIAPP structure to islet cell death remains elusive. Here we observe that hIAPP fibrils are cytotoxic to cultured pancreatic β -cells, leading us to determine the structure and cytotoxicity of protein segments composing the amyloid spine of hIAPP. Using the cryoEM method MicroED, we discover that one segment, 19–29 S20G, forms pairs of β -sheets mated by a dry interface that share structural features with and are similarly cytotoxic to full-length hIAPP fibrils. In contrast, a second segment, 15–25 WT, forms non-toxic labile β -sheets. These segments possess different structures and cytotoxic effects, however, both can seed full-length hIAPP, and cause hIAPP to take on the cytotoxic and structural features of that segment. These results suggest that protein segment structures represent polymorphs of their parent protein and that segment 19–29 S20G may serve as a model for the toxic spine of hIAPP.

DOI: [10.7554/eLife.19273.001](https://doi.org/10.7554/eLife.19273.001)

Introduction

Amyloid fibrils are associated with more than 25 diseases, including Alzheimer's disease, Parkinson's disease, and Type-II Diabetes (T2D) (Eisenberg and Jucker, 2012). The fibrils observed in each disease are composed of a particular protein; in T2D, amyloid fibrils are composed of human islet amyloid polypeptide (hIAPP) (Westermark et al., 1987; Cooper et al., 1988). hIAPP is a 37 residue

eLife digest In Type-II Diabetes, an individual's cells fail to respond correctly to the hormone insulin, leaving them unable to counteract high levels of sugar in the blood. Another hormone, human islet amyloid polypeptide (hIAPP), works with insulin to regulate blood sugar levels. hIAPP is an amyloid protein, which means that it can lose its normal structure and form fibrils. Fibrils are difficult for cells to break down and are often associated with disease. Indeed, fibrils of hIAPP often form in the pancreas as part of Type-II Diabetes.

Some studies have shown that hIAPP fibrils are toxic to pancreatic cells and worsen the symptoms of Type-II Diabetes. Others suggest that it is the process of fibril formation that is toxic, not the fibrils themselves. Although the structures of the fibrils have been described, whether these structures cause cell toxicity has not been investigated.

Krotee et al. have now explored the structures of two overlapping segments of hIAPP using a new cryo electron microscopy method called MicroED that is ideal for studying such segments. One segment, called 19-29 S20G, forms a standard amyloid fibril structure that is similar to the structure of full-length hIAPP fibrils. Adding these segments to human cells causes similar levels of toxicity as the full-length hIAPP fibrils. The second segment, called 15-25 WT, forms a non-toxic structure that is less stable than standard amyloid fibrils.

The results presented by Krotee et al. support the view that standard amyloid fibril structures are toxic to cells and suggest that 19-29 S20G may be a good model to use when studying how full-length hIAPP fibrils behave. The structure of 19-29 S20G may also be useful as a template for designing molecules that block amyloid fibril growth. If amyloid fibrils cause cell toxicity in the pancreas, then these molecules could be used to treat Type-II Diabetes.

DOI: [10.7554/eLife.19273.002](https://doi.org/10.7554/eLife.19273.002)

polypeptide hormone that is co-secreted with insulin to modulate glucose levels (**Roberts et al., 1989; Westermark et al., 2011**).

Researchers have accumulated substantial evidence for a correlation between hIAPP aggregation and pancreatic β -cell death in the course of the disease, T2D. Approximately 90% of pancreatic tissue samples taken post-mortem from T2D patients contain islet amyloid primarily composed of hIAPP (**Höppener et al., 2000**). The extent of islet amyloid positively correlates with pancreatic β -cell loss and insulin dependence (**Maloy et al., 1981; Esapa et al., 2005; Jurgens et al., 2011**). Additional support for a link comes from comparison of human and mouse IAPP: mouse IAPP differs from human IAPP by only six residues, 3 of which are β -strand breaking prolines. Consequently, mouse IAPP does not aggregate (**Nishi et al., 1989; Westermark et al., 1990**). Moreover, mice can be induced to develop islet amyloid and T2D when they are engineered to express human IAPP and fed a high fat diet (**Verchere et al., 1996; Westermark et al., 2000**). Perhaps the strongest support for a link is the mutation in hIAPP, hIAPP-S20G; segments that contain this mutation aggregate more quickly, contribute to increased pancreatic β -cell apoptosis, and are associated with early onset T2D in families who carry this lesion (**Sakagashira et al., 2000; Cao et al., 2012; Meier et al., 2016; Sakagashira et al., 1996; Lee et al., 2001; Morita et al., 2011**).

Although a link between hIAPP aggregation and pancreatic β -cell death is well established, precisely which type of hIAPP aggregate contributes to pancreatic β -cell death and insulin dependence remains undetermined. Using mostly in vitro studies, researchers have presented evidence for toxicity of multiple types of hIAPP aggregates. Early studies suggest that amyloid fibrils are the primary cytotoxic species because preparations that contain fibrillar hIAPP were more cytotoxic than soluble preparations of the protein (**Lorenzo et al., 1994; Lorenzo and Yankner, 1994; Schubert et al., 1995; Kapurniotu, 2001**). Using cells and transgenic rodents as disease models, other studies found hIAPP fibrils to be associated with apoptosis, β -cell loss, and T2D severity (**O'Brien et al., 1995; Hiddinga and Eberhardt, 1999; Janson et al., 1996; Hull et al., 2005a, 2005b; Pilkington et al., 2016**). In contrast, some studies show that the process of hIAPP fibril formation, not the amyloid fibrils themselves, is the source of toxicity (**Schlamadinger and Miranker, 2014; Oskarsson et al., 2015**). However, most current research studies suggest soluble pre-fibrillar oligomers are the primary type of toxic aggregate. Support for oligomers as the primary cytotoxic species comes from

the observation of oligomers associated with caspase activity and ER stress, which precede the formation of extracellular amyloid fibrils (Meier et al., 2006; Ritzel et al., 2007; Bram et al., 2014; Mukherjee et al., 2015; Lin et al., 2007; Huang et al., 2007; Haataja et al., 2008; Abedini et al., 2016). Several recent studies show that hIAPP fibrils are relatively inert and do not exert obvious toxicity. Despite these extensive in vitro studies, it is not clear that the toxic aggregates they describe also elicit toxicity in vivo.

In closer agreement with earlier studies, we find that hIAPP preparations that contain fibrils are cytotoxic to a rat pancreatic β -cell line, thus motivating us to determine the structure of the spine of hIAPP fibrils. If fibrils are a bona fide type of toxic aggregate in vivo, then determining the atomic structure of the spine of hIAPP fibrils is a logical approach for advancing our understanding of disease-relevant targets (Wiltzius et al., 2008, 2009a; Soriaga et al., 2016). Furthermore, we can utilize atomic structures as templates for structure-based design of novel therapeutics that may protect against pancreatic β -cell death. Although full-length amyloid proteins have so far been resistant to crystallization, select protein segments that form the spines of amyloid fibrils do form crystals (Nelson et al., 2005; Sawaya et al., 2007; Rodriguez et al., 2015). Indeed, the atomic structures of nearly 90 amyloid spines have been revealed in this manner. Other studies have taken an alternative approach: they employed solid-state NMR to gain detailed structural insights into hIAPP fibril structure (Luca et al., 2007; Weirich et al., 2016); some of these structures have spurred successful inhibitor designs (Mirecka et al., 2016). Here, we use the cryoEM method MicroED to determine the atomic structure of two 11-residue segments, termed spine segments, that span the amyloid spine of hIAPP.

Results

hIAPP preparations that contain fibrils are cytotoxic to cultured rat pancreatic β -cells

To compare the cytotoxic effects of oligomeric and fibrillar hIAPP, we generated hIAPP preparations that contained either amyloid oligomers or fibrils. We did this by aging the same concentration of hIAPP for 0 and 24 h time periods. Aging hIAPP for 24 h yielded amyloid fibrils and no detectable oligomers as assessed by Thioflavin-T (ThT) binding, negative-stain transmission electron microscopy (TEM), and a dot blot assay using the fibrillar oligomer-sensitive antibody, LOC (Figure 1A). Aging hIAPP for 0 h, which is a freshly dissolved hIAPP sample, yielded oligomers as assessed by a dot blot assay using LOC, and no amyloid fibrils (Figure 1—figure supplement 1A). Of note, we probed both hIAPP preparations with 25 different conformational antibodies that are known to bind soluble oligomers, but only LOC showed binding to any of our preparations. Although LOC was raised against hIAPP fibrils (Kayed et al., 2007), studies show that it also recognizes fibrillar oligomers (Wu et al., 2010), which share structural epitopes with amyloid fibrils and are structurally distinct from A11-positive pre-fibrillar oligomers.

We observe that hIAPP preparations that contain fibrils are significantly more cytotoxic to rat pancreatic β -cells than hIAPP preparations that contain oligomers but no detectable fibrils (Figure 1B and C). We assayed the cytotoxicity of the hIAPP preparations to Rin5F cells, a rat pancreatic β -cell line (Gazdar et al., 1980) using two metrics: 3-(4,5-dimethylthiazol-2-yl)-2,5-diphenyltetrazolium bromide (MTT) dye reduction, an indicator of good metabolic health (Mosmann, 1983; Liu et al., 1997), and activation of caspase-3/7, an indicator of apoptosis (Budihardjo et al., 1999). Furthermore, the insoluble fraction of the hIAPP 24 h sample, which contains fibrils (Figure 1—figure supplement 1B), is cytotoxic, while the soluble fraction is not (Figure 1D), further suggesting that fibrils are the toxic aggregate in our studies.

Although we do not detect oligomers in the 24 h sample, we cannot rule out the possibility that it may contain some undetectable population of slowly forming, yet highly toxic oligomers that associate with fibrils. Despite this possibility, we chose to focus on studying fibrillar structures of hIAPP.

Selection of amyloid spine segments for structural studies

Given that hIAPP fibrils are cytotoxic, we sought to identify the residues that compose their amyloid spine. We identified residues 15–29 as the amyloid spine based on several lines of evidence and previous work by others (Westermarck et al., 1990; Moriarty and Raleigh, 1999; Goldsbury et al.,

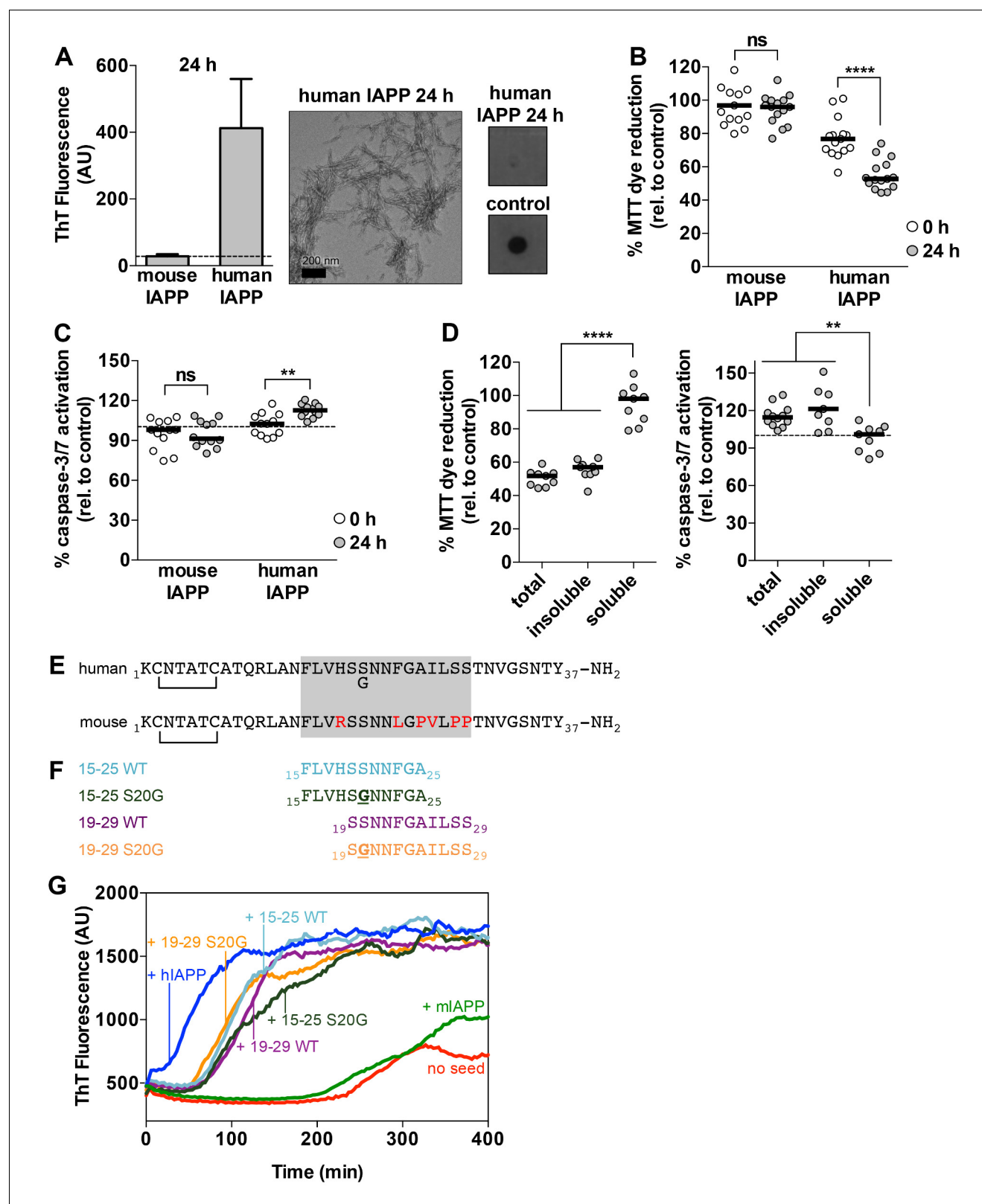


Figure 1. Preparations of hIAPP that contain amyloid fibrils are cytotoxic to a rat pancreatic β -cell line. (A) Human IAPP (hIAPP) aged for 24 h contains amyloid fibrils and no detectable oligomers. Amyloid fibrils were observed using ThT binding and TEM. Oligomers were detected using a dot blot assay with the polyclonal anti-oligomer antibody, LOC. hIAPP oligomers were used as the positive control for LOC binding. The dashed line on the ThT binding graph indicates ThT fluorescence of vehicle alone. (B) and (C) hIAPP aged for 24 h is significantly more cytotoxic than hIAPP aged for 0 h. In Figure 1 continued on next page

Figure 1 continued

these experiments, 50 μ M human and mouse IAPP were aged for the designated time periods and then they were applied to cells at 5 μ M final concentration. Mouse IAPP (mIAPP), which does not form amyloid fibrils, is not cytotoxic regardless of time period of aging. Black horizontal bars indicate the median ($n = 12$ – 15 across 4–5 biological replicates, each with three technical replicates). (B) Rin5F cells treated with hIAPP aged for 24 h reduce significantly less MTT dye than Rin5F cells treated with hIAPP aged for 0 h (ns=not significant; **** $p < 0.0001$ using an unpaired t-test with equal standard deviations). (C) Rin5F cells treated with hIAPP aged for 24 h exhibit significantly higher caspase-3/7 activation than Rin5F cells treated with hIAPP aged for 0 h. Additionally, Rin5F cells treated with hIAPP aged for 24 h exhibit significantly higher caspase-3/7 activation than vehicle-treated cells (** $p = 0.0008$ using an ordinary one-way ANOVA), but Rin5F cells treated with hIAPP aged for 0 h do not ($p = 0.4286$ using an ordinary one-way ANOVA) (ns=not significant; ** $p = 0.0011$ using an unpaired t-test with equal standard deviations). (D) The insoluble fraction of hIAPP aged 24 h, which contains amyloid fibrils and no detectable oligomers, contains the cytotoxic species. Cytotoxicity was measured using MTT dye reduction and detection of caspase-3/7 activation (**** $p < 0.0001$; ** $p < 0.0013$; $n = 9$ across three biological replicates, each with three technical replicates). (E) Amino acid sequences of human IAPP and mouse IAPP. The location of the early onset familial mutation, S20G, is shown below the human sequence. Red residues in the mouse sequence differ from the human sequence. The amyloid spine of human IAPP and the corresponding region in the mouse sequence is enclosed in the gray box. (F). Schematic of protein segments that span the amyloid spine, hereon referred to as spine segments, targeted for characterization. (G) Fibrils of spine segments seed hIAPP fibril formation, suggesting that spine segments embody structural characteristics of full-length hIAPP fibrils. 10 μ M hIAPP was seeded with 10% (v/v) monomer equivalent of pre-formed, unsonicated seed of each spine segment. mIAPP, which does not contain amyloid fibrils, does not seed hIAPP fibril formation. Curves show average of 4 technical replicates.

DOI: [10.7554/eLife.19273.003](https://doi.org/10.7554/eLife.19273.003)

The following figure supplements are available for figure 1:

Figure supplement 1. Characterization of hIAPP aged for 0 h and the soluble and insoluble fractions of hIAPP aged for 24 h.

DOI: [10.7554/eLife.19273.004](https://doi.org/10.7554/eLife.19273.004)

Figure supplement 2. All spine segments form amyloid fibrils or 3D crystals only a few hundred nanometers thick, as observed using TEM.

DOI: [10.7554/eLife.19273.005](https://doi.org/10.7554/eLife.19273.005)

Figure supplement 3. Technical replicates and control samples for ThT assay in **Figure 1G**.

DOI: [10.7554/eLife.19273.006](https://doi.org/10.7554/eLife.19273.006)

2000; Tenidis et al., 2000). First, the sequence of mouse IAPP (mIAPP), which is non-amyloidogenic, differs from human IAPP only within this region (**Figure 1E**). Second, the only known familial disease mutation in hIAPP, hIAPP-S20G, also occurs within this region (**Figure 1E**) (Sakagashira et al., 2000; Cao et al., 2012). Third, previous work by our laboratory has shown that Phe15 may be part of the amyloid spine because it is required for stabilizing an on-pathway α -helical dimer and mutating this residue can delay fibril formation (Wiltzius et al., 2009b).

For these reasons, we chose to focus on two overlapping 11-residue segments within this region of the sequence: residues 19–29 and residues 15–25. We chose to study the WT and early onset S20G mutation segments (**Figure 1F**). All four spine segments form amyloid fibrils or crystals (**Figure 1—figure supplement 2**) that seed full-length hIAPP fibril formation (**Figure 1G**, **Figure 1—figure supplement 3**), suggesting that the spine segments embody structural characteristics of full-length hIAPP fibrils.

Segment 19–29 S20G forms pairs of β -sheets tightly mated by a dry interface

To determine the structure of segment 19–29 S20G, we used Micro-Electron Diffraction (MicroED). MicroED employs a standard cryo electron microscope (cryoEM) in diffraction mode for data collection from 3D crystals only a few hundred nanometers thick (**Figure 2A**; **Figure 3A**) (Shi et al., 2013; Nannenga et al., 2014a, 2014b; Hattne et al., 2015; Liu et al., 2016). Such thin crystals are capable of producing measurable Bragg peaks because electrons interact with matter more strongly than X-rays. Indeed, we found that the nano-sized 3D crystals used for MicroED produced higher resolution diffraction than relatively larger crystals suited for structure determination at a microfocus X-ray beamline (**Figure 2A**). Evidently, micron-thick needle crystals are sufficient for X-ray structure determination with six or seven residue peptides, but not for 11-residue peptides. These experiences closely mirrored those in the determination of the atomic structure of the toxic core of α -synuclein (Rodriguez et al., 2015), an 11-residue segment that forms the spine of amyloid fibrils associated with Parkinson's disease.

The MicroED atomic structure of segment 19–29 S20G reveals pairs of parallel in-register β -sheets mated face-to-face by interdigitation of side-chains and exclusion of water molecules (**Figure 3B and C**; **Table 1**). This arrangement is termed a class I steric-zipper. Such features are observed for

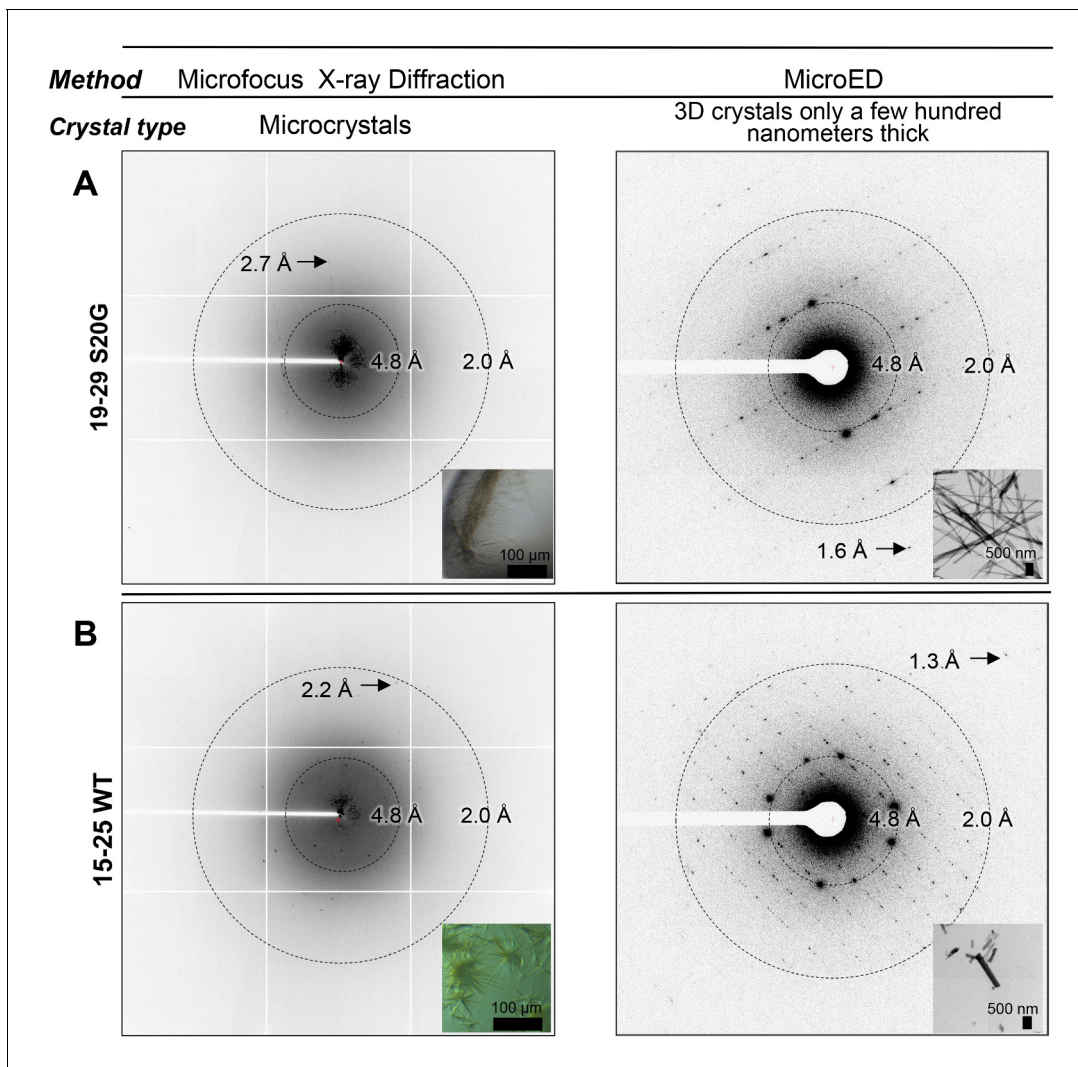


Figure 2. Bragg peaks produced by MicroED from 3D crystals only a few hundred nanometers thick are observed at higher resolution than peaks produced by X-ray diffraction at a microfocus beamline from microcrystals 10,000 times larger. (A) 3D crystals of 19–29 S20G (right, inset) diffract to 1.6 Å using MicroED, a whole angstrom better resolution than the microcrystals of 19–29 S20G (left, inset). (B) 3D crystals of 15–25 WT (right, inset) diffract to 1.4 Å using MicroED, whereas microcrystals of 15–25 WT diffract to 2.2 Å using Microfocus X-rays (left, inset).

DOI: 10.7554/eLife.19273.007

amyloid spines of other proteins and have been associated with pathology (Nelson et al., 2005; Sawaya et al., 2007; Ivanova et al., 2009; Colletier et al., 2011; Liu et al., 2011). This zipper contains a tightly packed hydrophobic core consisting of Phe23, Ala25, and Ile27. Phe23 is the central and largest contributor the hydrophobic core, consistent with multiple other experiments (Tenidis et al., 2000; Griffiths et al., 1995; Jack et al., 2006; Madine et al., 2008). The dry interface buries 265 Å² of surface area per strand, which equates to 24 Å² per residue. This interface is one of the largest and most complementary of any structurally determined steric-zipper interface (Supplementary file 1); it has a shape complementarity of 0.85. The dry interface is nearly as large as the toxic core of α -synuclein (Rodriguez et al., 2015), but with higher shape complementarity.

The β -sheets of the 19–29 S20G atomic structure possess a curvature that is not common in shorter hIAPP protein segments (Wiltzius et al., 2008, 2009a; Soriaga et al., 2015). To assess β -sheet curvature, we compared the root mean square deviations (RMSD's) of sheets from planarity across all hIAPP protein segment atomic structures determined to date (Supplementary file 1). The 19–29 S20G structure ranks in the upper half of the list (Figure 3—figure supplement 2), containing

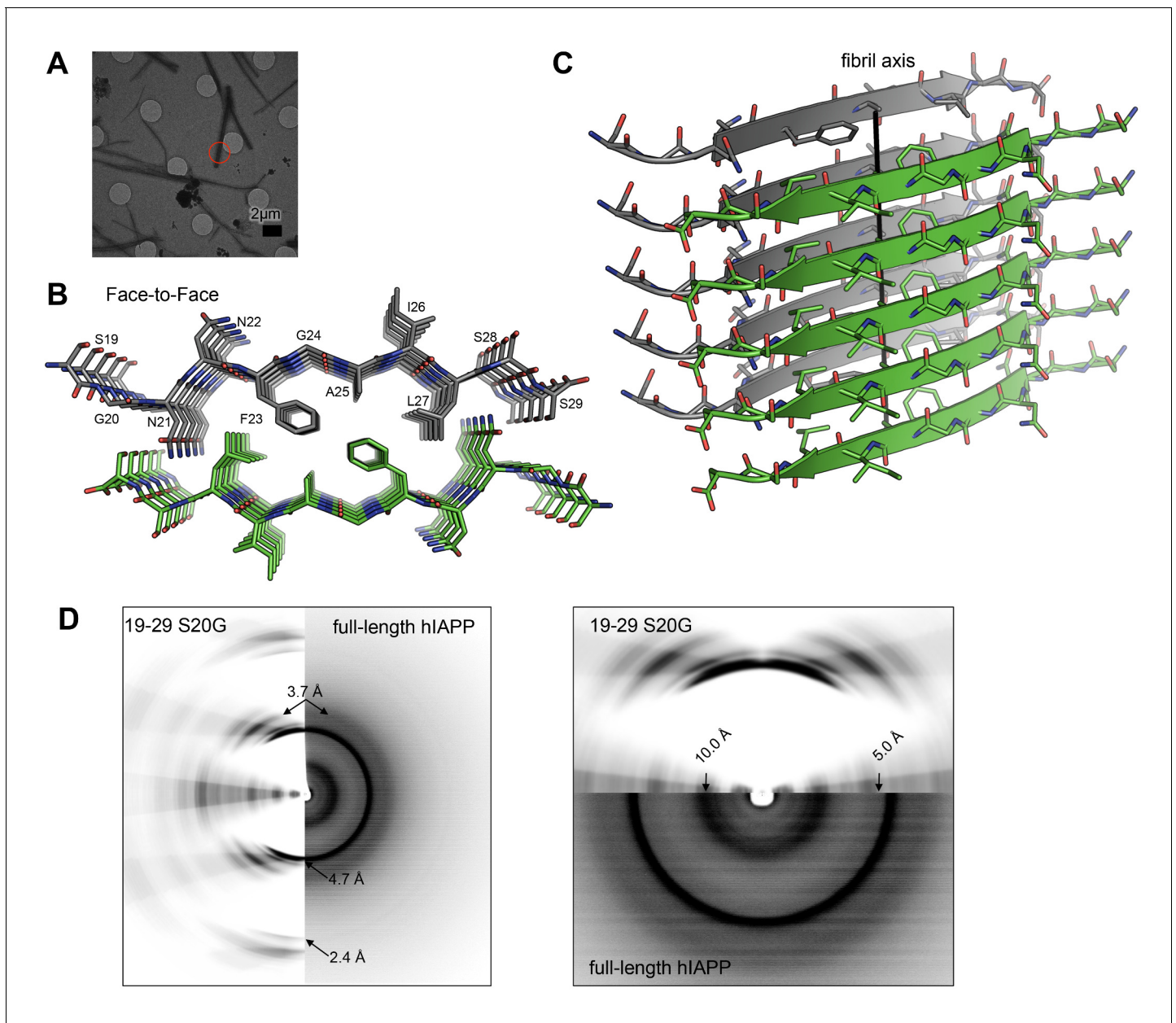


Figure 3. The MicroED atomic structure of segment 19–29 S20G reveals pairs of β -sheets mated by a dry interface. (A) Electron micrograph of 3D crystals used for data collection. The red circle represents the area of the crystal used for diffraction. (B) Pairs of β -sheets are oriented face-to-face and they are tightly mated by a dry interface that excludes water. The dry interface is formed by tightly packed, interdigitating side-chains. This panel shows 5 β -strands or layers along the 'a' dimension of the unit cell; the average crystal used for data collection is 10,400 layers long in the 'a' dimension. (C) Orthogonal view of the steric zipper formed by the dry interface. (D) The similarity between the fiber diffraction pattern calculated from the structure shown in Panel C and the fiber diffraction observed from full-length hIAPP fibrils supports the dry interface as a model for the amyloid spine of full-length hIAPP fibrils. Along the meridian (left panel), the dry interface and full-length hIAPP fibrils share reflections at 4.7 Å and 2.4 Å (black arrows). Additionally, along the off-meridional, the diffraction patterns share a reflection at 3.7 Å. It is difficult to see the reflection at 2.4 Å in the full-length hIAPP fiber diffraction image, but the reflection is clearly visible in the radial profile in **Figure 3—figure supplement 1**. Along the equator (right panel), the dry interface and full-length hIAPP fibrils share reflections at 10.0 Å and 5.0 Å (black arrows). The right panel is magnified 2X to more clearly show the low-resolution reflections along the equator.

DOI: [10.7554/eLife.19273.008](https://doi.org/10.7554/eLife.19273.008)

The following figure supplements are available for figure 3:

Figure supplement 1. The crystal packing of segment 19–29 S20G reveals a second interface, termed the 'Back-to-Back' or wet interface, which does not form the amyloid spine.

DOI: [10.7554/eLife.19273.009](https://doi.org/10.7554/eLife.19273.009)

Figure 3 continued on next page

Figure 3 continued

Figure supplement 2. Scatter plot of sheet RMSD from planarity values for all hIAPP protein segment structures determined to date.

DOI: [10.7554/eLife.19273.010](https://doi.org/10.7554/eLife.19273.010)

Figure supplement 3. 19–29 WT and S20G have similar fibrillar structures.

DOI: [10.7554/eLife.19273.011](https://doi.org/10.7554/eLife.19273.011)

Figure supplement 4. Radial profile calculated from the X-ray diffraction pattern given by cytotoxic full-length hIAPP fibrils.

DOI: [10.7554/eLife.19273.012](https://doi.org/10.7554/eLife.19273.012)

both sheet curvature and a sharp kink. Most of the shorter peptides are nearly flat, but some have sharp kinks. The significance of deviation from planarity is not yet clear.

The similarity between the fiber diffraction pattern calculated from this steric-zipper and the fiber diffraction pattern collected from full-length hIAPP fibrils tends to validate the 19–29 S20G atomic structure as a model for the amyloid spine of full-length hIAPP (**Figure 3D**). The diffraction patterns share several key features, including reflections at 4.7 Å and 2.4 Å along the meridian, a reflection at 3.7 Å along the off-meridian (left panel), and reflections at 10.0 Å and 5.0 Å along the equator (right panel).

Structural studies performed here and elsewhere by others suggest that 19–29 WT can form a similar dry interface to the one observed in the 19–29 S20G atomic structure. Radial profiles calculated from X-ray fiber diffraction of 19–29 WT and 19–29 S20G fibrils show strong reflections in common at 4.6 Å, 8.4 Å and 8.7 Å, and 34.7 Å, indicative of interstrand, intersheet, and proto-filament spacing, respectively (**Figure 3—figure supplement 3**). A previous study of 20–29 WT fiber diffraction revealed comparable reflections, which the authors used to formulate a fibril model of 20–29 WT that roughly agrees with our 19–29 S20G atomic structure (**Madine et al., 2008**). Our atomic structure and their model differ by a small shift in registration between sheets, allowing for tighter packing in the atomic structure. These results are consistent with earlier findings by Cao and co-workers, who observed that hIAPP-WT fibrils seed hIAPP-S20G fibril formation, thus suggesting a shared fibrillar structure (**Cao et al., 2012**).

Although the WT and mutant segments likely form similar structures, the structure of the mutant segment may be more stable. The stability of the mutant segment may stem from the early onset Gly20 mutation, which adopts an unusual geometry ($\phi = -101.7^\circ$ and $\psi = 107.5^\circ$) that creates a kink in the peptide backbone. To investigate this hypothesis, we generated a model of 19–29 WT consisting of a mated pair of ten-stranded sheets. The model was identical to the 19–29 S20G atomic structure with the exception that we adjusted the backbone torsion angles of Ser20 to comply with the allowed regions of the Ramachandran plot for a non-glycine residue. We compared the energies of the WT and S20G structures after minimization with FoldIt (**Cooper et al., 2010**). The dry interfaces are nearly identical between the two segments, except near Asn21, where the altered backbone torsion angles break the canonical Asn ladder hydrogen bonding interactions with neighboring Asn21 residues within the sheet and instead, form hydrogen bonds with Ser29 from the opposing sheet. The alteration separates the pair of sheets by approximately 1.5 Å in this region, and therefore the 19–29 S20G structure has a slightly lower energy than 19–29 WT (–590 REU vs. –535 REU).

Segment 15–25 WT forms an arrangement of labile unmated β -sheets

The atomic structure of segment 15–25 WT, also determined using MicroED (**Figure 2B**; **Figure 4A**), shows an arrangement of unmated β -sheets composed of anti-parallel out-of-register β -strands that is uncharacteristic of pathogenic amyloid fibrils (**Figure 4B**; **Table 1**). Most pathogenic amyloid fibrils are composed of β -strands that stack perpendicular to the sheet-long axis, but the β -strands in out-of-register structures stack at an angle. Deviation of strands from the fibril perpendicular is a natural consequence of the registration shift implied by out-of-register structures. The out-of-register β -strands are stabilized by extensive hydrogen bonding. Within each sheet, the β -strands form two distinct, unequal interfaces: a stronger interface with twelve hydrogen bonds, and a weaker interface with eight hydrogen bonds (**Figure 4B**). This inequality between interfaces has been observed in previous examples of out-of-register sheets (**Soriaga et al., 2015**; **Laganowsky et al., 2012**; **Liu et al., 2012**; **Yu et al., 2015**). A view down the ‘proto-fibril axis’ of the crystal shows that the faces of adjacent sheets are wet and overlap only partially (**Figure 4C**); the asymmetric unit contains density for seven ordered water molecules and one thiocyanate molecule. The area buried between

Table 1. Statistics of MicroED data collection and atomic refinement.

Sample	19–29 S20G	15–25 WT
Excitation Voltage (kV)	200	200
Electron Source	field emission gun	field emission gun
Wavelength (Å)	0.0251	0.0251
Total dose per crystal (e [−] / Å ²)	3.4	2.9
Frame rate (frame/s)	0.3–0.5	0.3–0.5
Rotation rate (°/s)	0.3	0.3
# crystals used	6	6
Total angular rotation collected (°)	68	68
Merging Statistics	19–29 S20G	15–25 WT
space group	P2 ₁ 2 ₁ 2 ₁	P1
Unit cell dimensions		
a, b, c (Å)	4.78, 18.6, 70.8	11.68, 18.18, 19.93
α, β, γ (°)	90, 90, 90	62.8, 88.9, 87.6
Resolution (Å)	1.9	1.4
R _{merge}	10.6% (15.0%)	19.9% (50%)
# of reflections	1380 (221)	9014 (153)
Unique reflections	548 (115)	2180 (84)
Completeness	83% (65%)	75% (35.3%)
Multiplicity	2.5 (1.9)	4.1 (1.8)
I/σ	5.65 (3.65)	4.33 (1.10)
CC _{1/2} (Diederichs, 2013)	98.9%	98.5%
Refinement Statistics	19–29 S20G	15–25 WT
Reflections in working set	546	2177
Reflections in test set	53	218
R _{work} [†]	22.75%	22.47%
R _{free}	27.49%	25.90%
RMSD bonds (Å)	0.01	0.008
RMSD angles (°)	1.2	1.2
Ramachandran (%) [‡]		
Favored	100	100
Allowed	0	0
Outliers	0	0
PDB ID code	5KNZ	5KOO
EMDB ID code	EMD-8272	EMD-8273

*Highest resolution shell shown in parenthesis.

[†] $R_{factor} = 100 \times \frac{\sum ||F_{obs}| - |F_{calc}||}{\sum |F_{obs}|}$

F_{calc} and F_{obs} are the calculated and observed structure factor amplitudes, respectively. R_{work} refers to the R_{factor} for the data utilized in the refinement and R_{free} refers to the R_{factor} for 10% of the reflections randomly chosen that were excluded from the refinement.

[‡]Percentage of residues in Ramachandran plot regions were determined using Molprobit (**Chen et al., 2010**).
DOI: [10.7554/eLife.19273.013](https://doi.org/10.7554/eLife.19273.013)

adjacent sheets is small (10.7 Å² per residue) compared to the average steric-zipper (20.1 Å² per residue). Hence, there is no dry interface between adjacent sheets in the crystal, and the structure seems labile compared to that of 19–29 S20G.

Consistent with our observation of unmated β -sheets in the atomic structure, we observe that 15–25 WT fibrils are relatively weak and reversible compared to 19–29 S20G fibrils, which possess a canonical pathogenic amyloid fibril architecture. Turbidity readings followed by negative-stain EM reveal that 15–25 WT fibrils completely disaggregate in the presence of heat and 1% SDS, but 19–29 S20G fibrils remain intact in up to 2% SDS (**Figure 4—figure supplement 1**).

Similar to 19–29 S20G, the 15–25 WT atomic structure reveals curved β -sheets. The sheets possess one of the highest RMSD's of sheets from planarity for any hIAPP protein segment structure determined to date (**Supplementary file 1, Figure 4—figure supplement 2**).

X-ray fiber diffraction and radial profile analysis of 15–25 WT and 15–25 S20G fibrils indicate they form structures similar to each other (**Figure 4—figure supplement 3**). Taken together with the X-ray fiber diffraction data from the 19–29 segments, we conclude that the early onset S20G mutation does not confer a fibril morphology distinguishable from wild-type.

Structural polymorphs elicit different cytotoxic effects

Next we investigated the cytotoxic effects of the spine segments in order to determine if any of them were similarly cytotoxic to full-length hIAPP preparations. Although the cytotoxic mechanism of hIAPP is not fully understood, several reports show hIAPP induces mitochondrial dysfunction, alters cell metabolism, and initiates activation of pro-apoptotic machinery (*Butler et al., 2003; Mulder and Ling, 2009; Zraika et al., 2010; Magzoub and Miranker, 2012; Tomasello et al., 2014*). Based on these findings, we tested the cytotoxicity of the spine segments using MTT dye reduction (*Mosmann, 1983; Liu and Schubert, 1997*) and a FRET-based biosensor to assay altered metabolism and pro-apoptotic machinery activation (*Paulsson et al., 2008*), respectively.

Using MTT dye reduction, we observe that the labile 15–25 fibrils are not cytotoxic to HEK293 cells (**Figure 5A**), whereas 19–29 S20G fibrils have comparable cytotoxicity to full-length hIAPP fibrils (**Figure 5B**). To verify the cytotoxic effects of each sample, we examined the morphology of the treated cells under a light microscope. Additionally, in the context of residues 19–29, the S20G segment is significantly more cytotoxic than the WT segment, consistent with parent full-length hIAPP (*Sakagashira et al., 2000; Meier et al., 2016*) (**Figure 5B**). We did not detect any oligomers present in the 15–25 WT or 19–29 S20G fibril samples using the LOC antibody (**Figure 5—figure supplement 1**).

Based on our examination of the insoluble and soluble fractions of the cytotoxic 19–29 S20G sample, we determine that the cytotoxicity of 19–29 S20G mainly resides in its fibrillar form. We tested the cytotoxicity of the total, insoluble and soluble fractions of the 19–29 S20G sample to HEK293 cells using MTT dye reduction. We observe that the insoluble fraction, which contains amyloid fibrils, is similarly cytotoxic to the total (**Figure 5C**), just as we observed with full-length hIAPP (**Figure 1D, Figure 1—figure supplement 1B**). These results suggest that 19–29 S20G may form the toxic spine of full-length hIAPP.

Further evidence that 19–29 S20G may form the toxic spine of full-length hIAPP comes from our observation that (–)-epigallocatechin gallate (EGCG), a flavanol known to mitigate full-length hIAPP cytotoxicity by preventing hIAPP from forming fibrils (*Meng et al., 2010*), also mitigates 19–29 S20G cytotoxicity by preventing it from forming fibrils (**Figure 5—figure supplement 2B and C**). We hypothesize that EGCG may mitigate fibril formation of full-length hIAPP and 19–29 S20G by binding to a common site, such as the dry interface of the amyloid spine. A previous study suggested EGCG may mitigate hIAPP fibril formation by binding hIAPP via hydrophobic interactions (*Young et al., 2015*). Indeed, EGCG does not prevent fibril formation of 15–25 WT, which does not possess a dry hydrophobic interface (**Figure 5—figure supplement 2D**). In addition, these results further support our conclusion that preparations of segment 19–29 S20G that contain fibrils are cytotoxic.

Next we tested whether the spine segments activate pro-apoptotic machinery using a FRET-based biosensor assay for monitoring caspase-3 activity in real-time (*Paulsson et al., 2008*). In this assay, CHO cells are stably transfected with a construct containing enhanced cyan fluorescent protein (ECFP) and enhanced yellow fluorescent protein (EYFP) fused by a DEVD linker. FRET signal is observed by exciting ECFP at 440 nm. In cells undergoing apoptosis, active caspase-3-like proteases target and cleave the DEVD linker, resulting in loss of FRET signal. Cell viability is measured by monitoring the ratio of 540 nm/480 nm, which reports loss of FRET signal and increased caspase-3 activity.

Using this system, we observe that segment 19–29 S20G elicits the most caspase-dependent cytotoxicity of the spine segments and segments 15–25 are not cytotoxic (**Figure 5D and E**). Segment 19–29 S20G is not as cytotoxic as full-length hIAPP in this assay, possibly because hIAPP interaction with heparan sulfate proteoglycans (HSPG) is important for apoptosis induction (**Oskarsson et al., 2015**), and residues 1–8, which are missing in all of the spine segments, are required for hIAPP binding to HSPG's.

Fibril seeds of 15–25 WT reduce the cytotoxicity of full-length hIAPP

Given that the spine segments seed full-length hIAPP fibril formation and that 19–29 S20G and 15–25 WT fibrils elicit different cytotoxic effects, we investigated whether seeding with either of the spine segments alters hIAPP cytotoxicity. To do this, we prepared seeded hIAPP at 10 μ M with 10% monomer equivalent of pre-formed seeds, the same conditions used in the ThT assay in **Figure 1G**. For all cytotoxicity assays, we dilute samples 1 to 10 to the concentration specified in culture medium containing pre-plated cells. Thus, we tested the cytotoxicity of seeded hIAPP at 1 μ M in order to preserve the conditions of the ThT assay.

Using MTT dye reduction, we observe that hIAPP seeded with non-toxic 15–25 WT fibrils is less cytotoxic than hIAPP alone, but hIAPP seeded with stable, toxic 19–29 S20G fibrils is similarly cytotoxic to hIAPP alone (**Figure 6**). Likewise, hIAPP seeded with stable, toxic 19–29 S20G fibrils is significantly more cytotoxic than hIAPP seeded with labile, non-toxic 15–25 WT fibrils (**Figure 6**). Seeds alone are not cytotoxic, indicating the cytotoxic effects we observe originate from the interaction of each seed with hIAPP and not the seed alone.

There are two possible explanations for the reduced cytotoxicity of the seeded 15–25 WT sample. First, the 15–25 WT seeds may seed a non-toxic species of full-length hIAPP, or second, the 15–25 WT seeds may interact with full-length hIAPP in some way that reduces its cytotoxicity.

X-ray fiber diffraction and radial profile analysis of the hIAPP fibrils used in the cytotoxicity assay reveal that fibrils formed by seeding with stable, toxic 19–29 S20G fibrils have a slightly tighter packing than fibrils formed by seeding with labile, non-toxic fibrils. hIAPP fibrils formed by seeding with stable, toxic 19–29 S20G fibrils exhibit reflections indicative of shorter equatorial Bragg spacings than hIAPP seeded with labile, non-toxic 15–25 WT fibrils (9.0 Å versus 10.0 Å) (**Figure 6—figure supplement 1**). The tighter packing of these fibrils may explain their enhanced cytotoxicity. Fiber diffraction could not be detected from seeds alone prepared under the same conditions.

Discussion

In 1901, when Dr. Eugene Opie first observed islet amyloid in post-mortem pancreata of T2D patients, he proposed a link between the islet amyloid and T2D (**Opie, 1901**). Over a century later, multiple studies have shown an unequivocal link between hIAPP aggregation and T2D, but uncertainty remains about which type of hIAPP aggregate contributes to pancreatic β -cell death. Although most recent in vitro studies suggest soluble oligomers are the primary type of toxic aggregate, here, we find hIAPP samples that contain fibrils alter pancreatic β -cell metabolism and activate pro-apoptotic caspases.

These findings motivated us to determine the structure of the spine of hIAPP fibrils and elucidate structural features important for hIAPP cytotoxicity. To improve our likelihood of crystallization and structure determination, we selected four protein segments that span the spine. We discovered that segment 19–29 S20G forms a pair of β -sheets mated at a dry interface, a structure that shares key features with full-length hIAPP fibrils as described in the following paragraph. What's more, the fibrillar form of 19–29 S20G is cytotoxic. In contrast, segment 15–25 WT forms an unusual arrangement of single, out-of-register β -sheets that are not cytotoxic. The divergence in structure and cytotoxicity of segments 19–29 S20G and 15–25 WT suggests that strong, stable intermolecular interactions are important features of cytotoxic amyloid proteins.

The experiments of this study show that the 19–29 S20G atomic structure recapitulates many of the structural features and cytotoxic properties of hIAPP. First, preparations of 19–29 S20G that contain fibrils are cytotoxic, as is the case for full-length hIAPP. Second, X-ray fiber diffraction calculated from the dry interface of the 19–29 S20G atomic structure shares key features with fiber diffraction collected from full-length hIAPP fibrils. Third, segment 19–29 S20G elicits cytotoxicity by altering cell metabolism and activating pro-apoptotic machinery, mechanisms by which full-length hIAPP fibrils

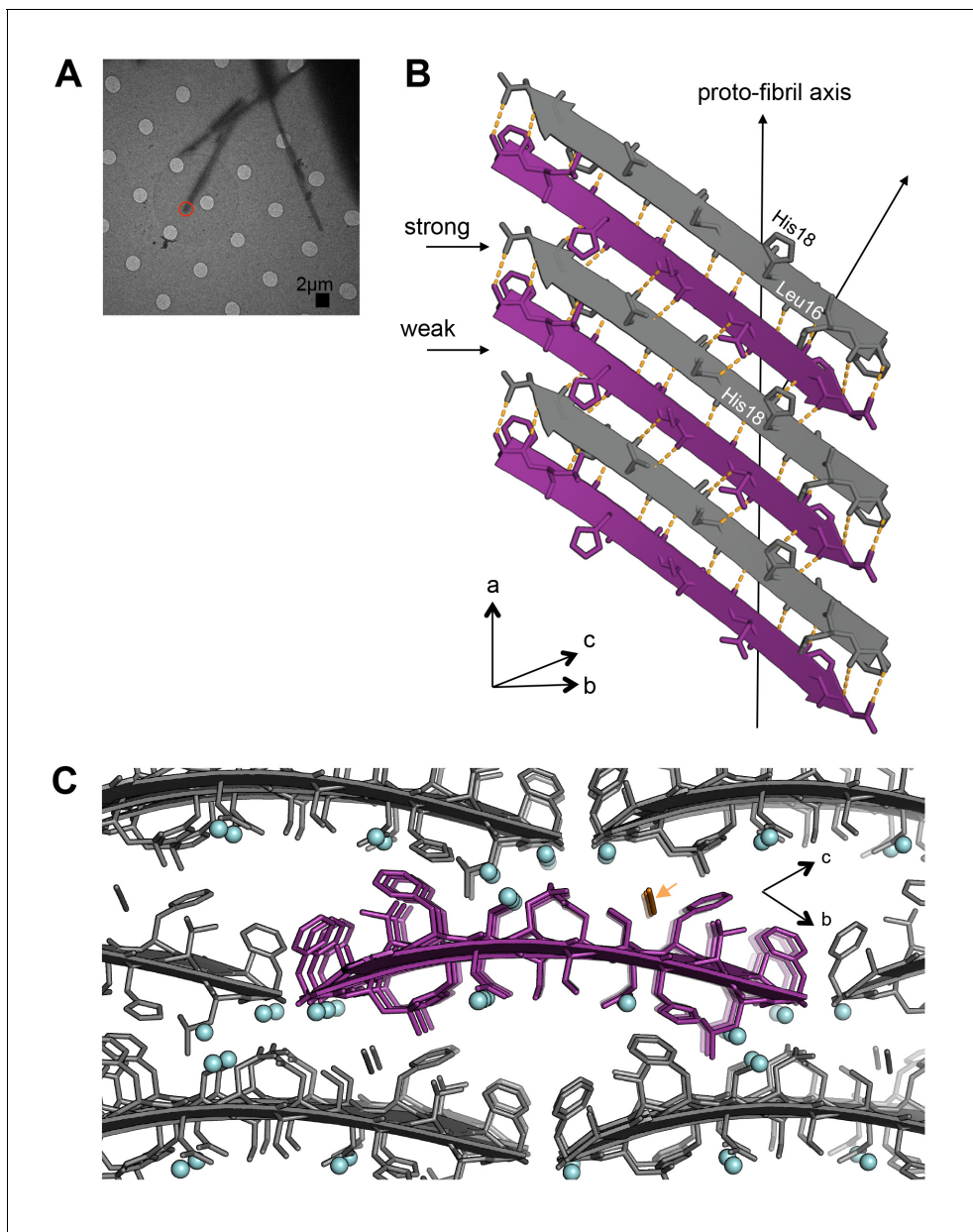


Figure 4. Segment 15–25 WT forms an arrangement of unmated β -sheets that is uncharacteristic of pathogenic amyloid fibrils. (A) Electron micrograph of 3D crystals used for data collection. The red circle represents the area of the crystal used for diffraction. (B) A single β -sheet contains anti-parallel out-of-register β -strands stabilized by two distinct, unequal interfaces: a stronger interface with twelve hydrogen bonds, and a weaker interface with eight hydrogen bonds. The β -strands are out-of-register by two residues because Leu16 on the first β -strand is directly above His18 on the third β -strand. (C) The view down the proto-fibril axis reveals hydrated interfaces between partially overlapping β -sheets. Notice that adjacent β -sheets lack side-chain interdigitation. Water molecules are shown as cyan spheres. The thiocyanate molecule is highlighted in gold in the central β -sheet and colored gray in the peripheral β -sheets.

DOI: [10.7554/eLife.19273.014](https://doi.org/10.7554/eLife.19273.014)

The following figure supplements are available for figure 4:

Figure supplement 1. 15-25 WT fibrils are relatively weak and reversible compared to 19–29 S20G fibrils.

DOI: [10.7554/eLife.19273.015](https://doi.org/10.7554/eLife.19273.015)

Figure supplement 2. Scatter plot of sheet RMSD from planarity values for all hIAPP protein segment structures determined to date.

DOI: [10.7554/eLife.19273.016](https://doi.org/10.7554/eLife.19273.016)

Figure supplement 3. 15-25 WT and S20G have similar fibrillar structures.

DOI: [10.7554/eLife.19273.017](https://doi.org/10.7554/eLife.19273.017)

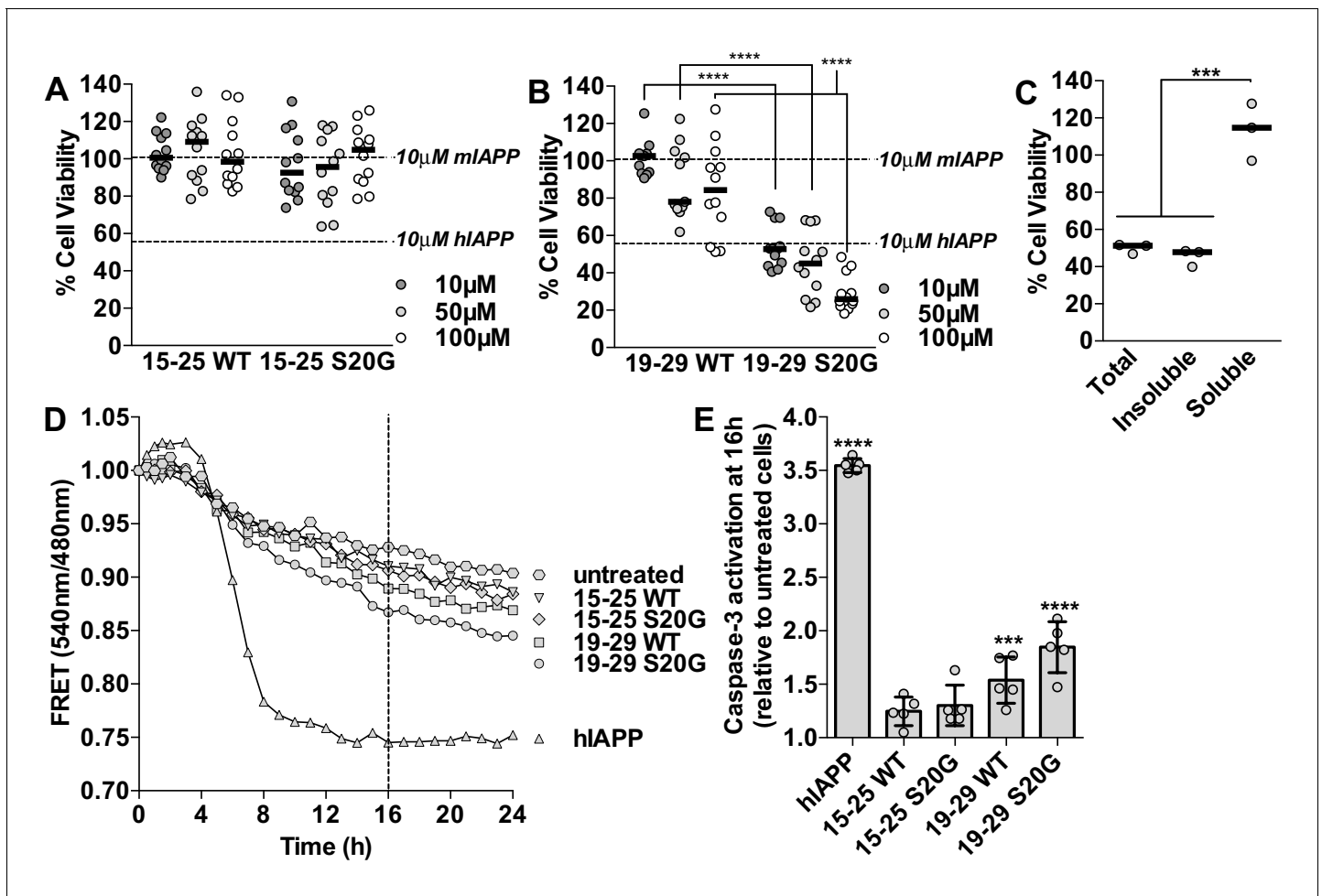


Figure 5. Segment 19–29 S20G forms the toxic core of hIAPP and segments 15–25 are not toxic. (A and B) Fibrils were formed by incubating the spine segments overnight under quiescent conditions, the same conditions used to prepared full-length hIAPP fibrils. Next, the samples were applied to HEK293 cells at the specified concentrations and then cell viability was quantified using MTT dye reduction. Bars show median cell viability; dashed lines show median cell viability from 10 μM mIAPP and hIAPP. (A) 15–25 WT and 15–25 S20G fibrils are not toxic compared to full-length hIAPP fibrils ($n = 12$ across four biological replicates, each with three technical replicates). (B) 19–29 WT fibrils are mildly cytotoxic and 19–29 S20G fibrils are significantly more cytotoxic than 19–29 WT fibrils (**** $p < 0.0001$ using a Mann-Whitney U test; $n = 12$ across four biological replicates, each with three technical replicates). 19–29 S20G fibrils (10 μM) are similarly cytotoxic to full-length hIAPP fibrils at the same concentration (lower dashed line) ($p = 0.09$ using an unpaired t-test with equal standard deviations). (C) The insoluble fraction of the 50 μM 19–29 S20G cytotoxic preparation contains the cytotoxic species. 19–29 S20G fibrils were formed overnight at room temperature and then pelleted by centrifugation. The soluble fraction was carefully removed and then filtered to ensure it contained no insoluble material. The insoluble material was resuspended in its original volume. Each sample was applied to HEK293 cells and then cell viability was quantified with MTT dye reduction (*** $p < 0.0002$ using an ordinary one-way ANOVA; $n = 3$ technical replicates) (D) and (E) Using a FRET-based biosensor assay for monitoring caspase-3 activity in real-time, 19–29 S20G fibrils induce the most caspase-3 activity, whereas segments 15–25 did not induce caspase-3 activity, consistent with the MTT dye reduction assay results. 50 μM of each spine segment seeded with 166 nM seeds was applied to stably transfected CHO cells. (D) Fold difference was recorded over 24 h. Datapoints represent average fold difference. The dashed line represents the 16 h mark. (E) Average levels of caspase-3 activation after a 16 h incubation relative to untreated cells (*** $p < 0.0002$; **** $p < 0.0001$ using an ordinary one-way ANOVA, Bonferroni correction; $n = 5$ technical replicates).

DOI: [10.7554/eLife.19273.018](https://doi.org/10.7554/eLife.19273.018)

The following figure supplements are available for figure 5:

Figure supplement 1. Fibrillar samples of 15–25 WT and 19–29 S20G do not contain detectable amyloid oligomers.

DOI: [10.7554/eLife.19273.019](https://doi.org/10.7554/eLife.19273.019)

Figure supplement 2. (–)-epigallocatechin gallate (EGCG), a flavanol known to mitigate full-length hIAPP cytotoxicity by preventing it from forming fibrils, likewise mitigates 19–29 S20G cytotoxicity by preventing it from forming fibrils.

DOI: [10.7554/eLife.19273.020](https://doi.org/10.7554/eLife.19273.020)

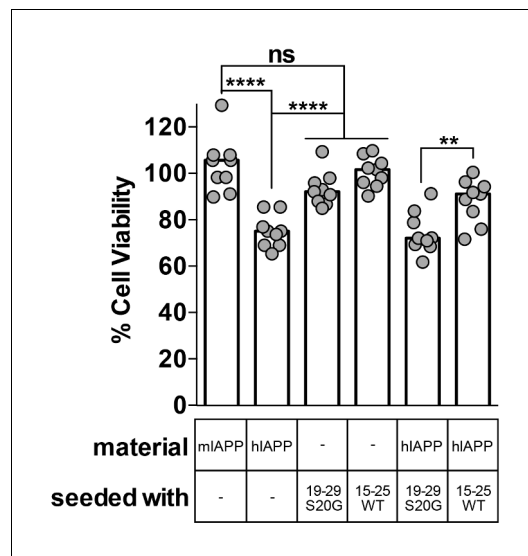


Figure 6. Fibril seeds of 15–25 WT reduce the cytotoxicity of full-length hIAPP. In this experiment, we incubated 10 μ M hIAPP with or without 10% monomer equivalent of pre-formed seeds overnight under quiescent conditions, the same conditions used to seed full-length hIAPP fibril formation in **Figure 1**. Next, we diluted the samples 1 to 10 in culture media containing pre-plated Rin5F cells. Note: the concentration of IAPP used in this experiment is less than the IAPP concentrations used in the cytotoxicity assays in **Figures 1** and **5**. hIAPP seeded with stable, toxic 19–29 S20G fibrils is more cytotoxic to Rin5F cells than hIAPP seeded with labile, non-toxic 15–25 WT fibrils. Columns indicate median cell viability (ns = not significant; ** $p=0.006$; **** $p<0.0001$ using an unpaired t-test with equal standard deviations, $n=9$ across three biological replicates, each with three technical replicates). 19–29 S20G seeds and 15–25 WT seeds (100 nM each) are not cytotoxic to Rin5F cells.

DOI: [10.7554/eLife.19273.021](https://doi.org/10.7554/eLife.19273.021)

The following figure supplement is available for figure 6:

Figure supplement 1. hIAPP fibrils made by seeding with each spine segment have slightly different structural features.

DOI: [10.7554/eLife.19273.022](https://doi.org/10.7554/eLife.19273.022)

are thought to contribute to pancreatic β -cell death during T2D. Fourth, the early onset S20G mutation confers greater cytotoxicity within segment 19–29 and within full-length hIAPP. Last, EGCG, a flavanol that mitigates full-length hIAPP fibril formation and cytotoxicity, likewise mitigates 19–29 S20G fibril formation and cytotoxicity. These results, taken together with the canonical pathogenic amyloid fibril architecture of segment 19–29 S20G, suggest it represents the toxic amyloid spine of hIAPP.

Our studies begin to provide a framework for understanding which hIAPP fibril polymorphs may contribute to pancreatic β -cell death during T2D. Previous structural studies of hIAPP protein segments (Wiltzius et al., 2008, 2009a; Soriaga et al., 2015) and full-length hIAPP (Luca et al., 2007; Weirich et al., 2016; Goldsbury et al., 1997; Kajava et al., 2005; Bedrood et al., 2012; Wineman-Fisher et al., 2015) identified an array of structures with diverse side-chain and sheet arrangements; the 15 hIAPP protein segment structures that overlap the hIAPP amyloid spine belong to six different steric-zipper classes (Figure 7). These multiple diverse structures suggest there is significant polymorphism within the hIAPP amyloid spine, but exactly which of these polymorphs elicit cytotoxicity was not known. By studying the structures and cytotoxic effects of protein segments in parallel, we identify a cytotoxic hIAPP fibril structure that may contribute to pancreatic β -cell death during T2D. Additionally, our studies suggest that not all hIAPP fibril structures are cytotoxic.

Both atomic structures presented here reveal a new and potentially important observation: curved β -sheets. In the dry interface of the 19–29 S20G atomic structure, the curved β -sheets accommodate the tightly packed hydrophobic core, which includes a bulky phenylalanine, while maintaining high shape complementarity and large buried surface area. Paradoxically, in the 15–25 WT atomic structure, the curved β -sheets appear to have an opposite effect: the curved β -

sheets appear to prevent adjacent sheets from associating to form a canonical pathogenic amyloid fibril architecture. In both atomic structures, the effect of the curved β -sheets is dictated by the registry of adjacent β -sheets (Supplementary file 1, Figure 7).

The 15–25 WT atomic structure joins the recently discovered class of out-of-register protein segment structures, which exert disparate cytotoxic effects. Here, we show that 15–25 WT is not cytotoxic but in contrast, the out-of-register protein segment KDWSFY from β 2-microglobulin elicits mild cytotoxicity (Liu et al., 2012). One notable difference between the two structures is that the 15–25 WT structure is formed of single sheets, while the KDWSFY structure is formed of sheets mated by a dry interface. The dry interface of the KDWSFY atomic structure results in a higher solvation energy per strand compared to the 15–25 WT atomic structure (122 cal/mol/strand vs. 19 cal/mol/strand). Given that cytotoxic structures like 19–29 S20G have relatively high solvation energies per strand

⁸ ATQRLANFLVHSSNNFGAILSSSTNVGSNTY ₃₇	Zipper symmetry class	Parallel (//) Or Anti-Parallel (A//)	Registry
G			
ANFLVH.....	2	//	in
NFLVHS.....	7	A//	in
NFLVHSS.....	6	A//	in
FLVHSSNNFGA.....	6	A//	out
LVHSSN.....	7	A//	in
HSSNNF.....	4	//	in
S GNNFGAILSS.....	1	//	in
NNFGAIL.....	1	//	in
NFGAILS.....	7	A//	out
FGAILSS.....	6	A//	in
AILSST.....	8	A//	in
SSTNVG.....	1	//	in
NVGSNTY.....	1	//	in

Figure 7. Schematic of structural features of all hIAPP protein segment structures determined to date. Parallel (//) or Anti-parallel (A//) refers to the orientation of β -strands within β -sheets. Registry refers to the translational offset of β -sheets perpendicular to the fiber axis.
DOI: 10.7554/eLife.19273.023

(279 cal/mol/strand; **Supplementary file 1**), this difference may explain the disparate cytotoxic effects of the two out-of-register structures. However, we need more studies of out-of-register protein structures and their cognate cytotoxic effects to definitively make this conclusion. The disparate cytotoxic effects within this structure class lead us to believe that the nature of cytotoxicity is not simply conferred by in-register or out-of-register structures. As many studies have suggested, there may be more than one mechanism of amyloid-related toxicity and the different mechanisms may be catalyzed by different architectures. Alternatively, maybe if additional residues were included, the anti-parallel out-of-register fiber could be stabilized, thereby increasing its toxicity.

Although the 19–29 WT fibrils prepared in this study appear morphologically similar to 19–29 S20G fibrils, the 19–29 WT fibrils are likely polymorphic and may contain some fraction of fibrils that are structurally similar to non-toxic 15–25 WT fibrils. Previous structural studies of segment 20–29 WT fibrils show that it forms an array of polymorphs, some of which are similar to the 15–25 WT atomic structure (Griffiths et al., 1995; Jack et al., 2006; Madine et al., 2008; Ashburn et al., 1992; Nielsen et al., 2009). Structural polymorphism of 19–29 WT fibrils may explain their lower cytotoxicity than 19–29 S20G fibrils, which are homogenous in structure.

These findings, expedited by MicroED, may inform our understanding of hIAPP fibril structures that contribute to pancreatic β -cell death in Type-II Diabetes patients. Going forward, we can use our toxic amyloid spine model as a template for structure-based design in the effort to develop much needed therapeutics that protect against pancreatic β -cell death and disease progression (Sievers et al., 2011; Kahn et al., 2014). In addition, if hIAPP fibrils truly are a major type of toxic aggregate that contributes to T2D, then raising antibodies against hIAPP fibrils may represent a

promising strategy for therapeutic development, especially in light of the recent success of preliminary studies with antibodies raised against amyloid- β (Sevigny *et al.*, 2016).

Materials and methods

IAPP and protein segments

Human IAPP(1–37)-NH₂ wild-type and mouse IAPP(1–37)NH₂ wild-type were synthesized by Innoprep (San Diego, CA) and CS Bio (Menlo Park, CA) and purified to greater than 98% purity. Human and mouse IAPP were prepared by dissolving the lyophilized proteins at 0.25–1 mM in 100% HFIP and leaving them to dissolve for several hours to ensure complete solubility. Next, the HFIP was removed with a CentriVap Concentrator (Labconco, Kansas City, MO). After removal of the HFIP, the peptides were dissolved at 1 mM, 5 mM, or 10 mM in 100% DMSO. The DMSO peptide stocks were diluted 100-fold in filter-sterilized Dulbecco's PBS (Cat. # 14200–075, Life Technologies, Carlsbad, CA). Samples were incubated at room temperature for the designated time periods.

All four spine segments were synthesized by GenScript (Piscataway, NJ) and purified to greater than 98% purity. Fibrils were formed by dissolving lyophilized peptide at 1 mM in PBS and 1% DMSO.

Crystallization

15-FLVHSSNNFGA-25 (15–25 WT). 15–25 WT was dissolved at 20 mg/ml in ice-cold, nano-pure water and then spin-filtered. Crystals were grown using the hanging drop vapor diffusion method at 4°C in 0.35 M NaSCN and 35% MPD. Crystals grew within several hours and reached maximum size in a week. 3D crystals only a few hundred nanometers thick grew alongside microcrystals in the same drops.

19-SGNNFGAILSS-29 (19–29 S20G). Microcrystals were grown using the hanging drop vapor diffusion method at 30°C in 0.2M acetate salts and 40% MPD. 3D crystals only a few hundred nanometers thick were grown in batch by dissolving lyophilized peptide at 1 mM in PBS and 1% DMSO without seeding. Crystals grew on the bench top at room temperature in several hours.

MicroED data collection

The procedures for MicroED data collection and processing largely follow published procedures (Hattne *et al.*, 2015; Shi *et al.*, 2016). Briefly, a 2–3 μ L drop of crystals in suspension was deposited onto a Quantifoil holey-carbon EM grid then blotted and vitrified by plunging into liquid ethane using a Vitrobot Mark IV (FEI, Hillsboro, OR). Blotting times and forces were optimized to keep a desired concentration of crystals on the grid and to avoid damaging the crystals. Frozen grids were then either immediately transferred to liquid nitrogen for storage or placed into a Gatan 626 cryo-holder for imaging. Images and diffraction patterns were collected from crystals using an FEG-equipped FEI Tecnai F20 TEM operating at 200 kV and fitted with a bottom mount TVIPS TemCam-F416 CMOS-based camera. Diffraction patterns were recorded by operating the detector in a movie mode termed 'rolling shutter' with 2 \times 2 pixel binning (Nannenga *et al.*, 2014b). Exposure times for these images were either 2 or 3 s per frame. During each exposure, crystals were continuously unidirectionally rotated within the electron beam at a fixed rate of 0.3 degrees per second, corresponding to a fixed angular wedge of 0.6 or 0.9 degrees per frame.

Crystals that appeared visually undistorted and that were 100–300 nm thick produced the best diffraction. Datasets from individual crystals were merged to improve completeness and redundancy. Each crystal dataset spanned a wedge of reciprocal space ranging from 40–80°. We used a selected area aperture of approximately 1 μ m. The geometry detailed above equates to an electron dose rate of less than 0.01 e[−]/Å² per second being deposited onto our crystals.

Measured diffraction images were converted from TVIPS format into SMV crystallographic format, using in-house software (available for download at <http://cryoem.janelia.org/downloads>) (Hattne *et al.*, 2015).

We used XDS to index and integrate the diffraction images and XSCALE (Kabsch, 2010) for merging and scaling together datasets originating from different crystals.

For 19–29 S20G, data from six crystals were merged to assemble the dataset used for molecular replacement. Of note, the resolution was cut off at 1.9 Å to facilitate subsequent rounds of structure refinement.

For, 15–25 WT, data from six crystals were merged to assemble the dataset used for molecular replacement. Of note, the diffraction pattern from the 15–25 WT crystals diffracted with MicroED reveal a pseudo two-fold symmetry. In line with this observation, we indexed and integrated the diffraction images with space group C2, but the datasets had relatively poor statistics compared to the P1 datasets and our attempts at refining molecular replacement solutions from the C2 datasets failed.

Structure determination

19–29 S20G. We determined the structure using molecular replacement. An idealized 7-residue poly-alanine strand led us to our atomic model. The solution was identified using Phaser (McCoy, 2007). A dataset merged from six crystals was used to identify the initial model, but subsequent rounds of model building and refinement were carried out using a dataset from a single crystal. Free R flags were copied over from the dataset merged from six crystals to the single crystal dataset. Subsequent rounds of model building and refinement were carried out using COOT and Phenix, respectively (Emsley and Cowtan, 2004; McCoy et al., 2005). Electron scattering factors were used for refinement.

15–25 WT. We determined the structure using molecular replacement. Dozens of search models were used, but an out-of-register β -strand model led us to our solution. The solution was identified using Phaser (McCoy, 2007). Subsequent rounds of model building and refinement were carried out using COOT and Phenix, respectively (Emsley and Cowtan, 2004; McCoy et al., 2005). Electron scattering factors were used for refinement. To aid in model building, we used a feature enhanced map (FEM), which sharpens B factors at high resolution (Afonine et al., 2015).

Calculations of the area buried and shape complementarity (SC) were performed with AREAIMOL (Lee and Richards, 1971; Collaborative Computational Project, Number 4, 1994) and SC (Connolly, 1983; Richards, 1977; Lawrence and Colman, 1993), respectively.

ThT binding

30 μ L of human and mouse IAPP preparations used in the cytotoxicity assays in Figure 1 were pipetted into a black-wall 384-well plate and then mixed with 3 μ L of 1 mM Thioflavin-T (ThT). Fluorescence was recorded with an excitation wavelength of 444 nm and an emission wavelength of 482 nm.

Dot blot assay

1 μ L of each sample generated for cytotoxicity assays in Figure 1 and Figure 5A and B was applied to a nitrocellulose membrane (Cat. # 162–0146, BioRad, Hercules, CA). Next, the membrane was blocked in 5% (w/v) nonfat dry milk in PBS-T (T = 0.1% (v/v) Tween-20 (Cat. #BP337-500, Fisher)) for 1 hr at room temperature. After blocking, the membrane was incubated with a 1:100 dilution of LOC polyclonal rabbit serum (Pacific Immunology, Ramona, CA) in 5% (w/v) milk in PBS-T at 4°C overnight. The membrane was washed in PBS-T for 10 min three times, and then incubated with anti-rabbit secondary antibody (RRID:AB_2307391; Cat. #111-035-144, Jackson ImmunoResearch, West Grove, PA) diluted 1:10,000 in PBS-T for 1 hr at RT. The membrane was washed three more times, and then the signal was developed with Clarity Western ECL Substrate (Cat. #170–5061, BioRad) and documented with a CCD camera. Exposures ranging from 5 s to 5 min were collected, but the 5 min exposure was used in all figures.

Imaging and negative stain transmission electron microscopy

Samples were spotted onto grids (holey or non-hole) and allowed to settle on the grid for 160 to 180 s. Remaining liquid was wicked off and grids were left to dry before analyzing. Sample grids were analyzed on the TF20 Electron Microscope (FEI, Hillsboro, OR). Images were collected at 3500 or 6000x magnification with an additional 1.4x post-column magnification and recorded using a TIETZ F415MP 16 megapixel CCD camera.

Samples for negative-stain EM were spotted on non-hole carbon-coated grids and allowed to settle on the grid for 160 to 180 s. Remaining liquid was wicked off and then 2% uranyl acetate was applied to the grid. After 1 min, the uranyl acetate was wicked off. The grids were left to dry before analyzing on the T12 Electron Microscope (FEI). Images were collected at 3,200 or 15,000x magnification and recorded using a Gatan 2kX2k CCD camera.

Cell culture

Rin5F cells were purchased from ATCC (RRID:CVCL_2177; Cat. # CRL-2058, Manassas, VA). Cells were cultured in RPMI media (ATCC, Cat. # 30-2001) plus 10% heat-inactivated fetal bovine serum. Cells were cultured at 37°C in a 5% CO₂ incubator. They tested negative for mycoplasma using a MycoAlert PLUS Detection Kit (Cat. #: LT07-701, Lonza, Switzerland) and they were authenticated using Cytochrome C Oxidase 1 (COX1) gene analysis by Laragen (Culver City, CA).

HEK293 c18 cells (hereon referred to as HEK293) were a gift from Carol Eng in the laboratory of Arnold J. Berk at UCLA, but they were originally purchased from ATCC (RRID:CVCL_6974). Cells were cultured in DMEM media (Cat. # 11965-092, Life Technologies) plus 10% heat-inactivated fetal bovine serum and 1% pen-strep (Life Technologies). Cells were cultured at 37°C in a 5% CO₂ incubator. They tested negative for mycoplasma using a MycoAlert PLUS Detection Kit and they were authenticated using STR profiling (Laragen).

CHO cells were purchased from ATCC (RRID:CVCL_0214; Cat. #: CCL-61). Cells were cultured in RPMI 1640 with 11 mM glucose (Sigma) with 10% FBS, and 1% pen-strep. Cells were cultured at 37°C in a 5% CO₂ incubator. They tested negative for mycoplasma using a PCR-based method and they were authenticated using mRNA analysis.

Spine segment fibril formation

Spine segments were dissolved at 1 mM in PBS with 1% DMSO. Samples were incubated at room temperature for 15 hr or up to one week under quiescent conditions to form fibrils. The presence of fibrils was confirmed with electron microscopy. Fibril samples were diluted appropriately for cell viability assays and fibril formation assays.

Fiber diffraction and radial profile analysis

Fibrils were spun down and washed with water three times to remove any salt. Fibrils of spine segments were spun down using a tabletop microfuge. Full-length hIAPP fibrils and spine segment seeds were spun down using an Airfuge Ultracentrifuge set at 75,000 rpm for 1 hr (Beckman-Coulter, Brea, CA). The samples were concentrated 10x in water and applied between two capillary ends and then the samples were left to dry overnight. Dried fibrils of spine segments and full-length hIAPP in **Figure 3D** were analyzed with a RIGAKU R-Axis HTC imaging plate detector using Cu K(alpha) radiation from a FRE+ rotating anode generator with VARIMAX HR confocal optics (Rigaku, Tokyo, Japan). Fiber diffraction from full-length hIAPP fibrils used in **Figure 6** was recorded by an ADSC Q315 CCD detector at the Advanced Photon Source 24-ID-E beamline (Argonne, IL).

Radial profiles were calculated using a program written in-house. The program calculates the average intensity as a function of distance from the beam center.

Thioflavin-T assays

Thioflavin-T (ThT) assays were performed in black 96-well plates (Nunc, Rochester, NY) sealed with UV optical tape. hIAPP and mIAPP were dissolved at 1 mM in 100% HFIP. The peptides were then diluted 100-fold in 20 mM sodium acetate pH 6.5 and 10 μM ThT. Unsonicated fibril seeds were added at 1 μM monomer equivalent concentration (10% v/v). ThT fluorescence was recorded with excitation and emission of 444 nm and 482 nm, respectively, using a SpectraMax M5 (Molecular Devices, Sunnyvale, CA). Experiments were performed in quadruplicate and readings were recorded every 3 min.

Model building and energy analysis of 19–29 WT and 19–29 S20G

To investigate whether 19–29 WT could form a similar structure to 19–29 S20G, we modeled a serine at position 20 in the 19–29 S20G atomic structure. We adjusted the backbone torsion angles so that they fell within the 'allowed' regions of the Ramachandran plot for a non-glycine residue

(Emsley and Cowtan, 2004). We performed energy minimization using FoldIt (RRID:SCR_003788) (Cooper et al., 2010) and compared the energies of the resulting models of 19–29 WT and 19–29 S20G.

Cytotoxicity assays

HEK293 cells and Rin5F cells were plated at 10,000 and 27,000 cells per well in 90 μ L, respectively, in 96-well plates (Cat. # 3596, Costar, Tewksbury, MA). Cells were allowed to adhere to the plate for 20–24 hr.

For the assay in **Figures 1** and 50 μ M full-length IAPP was aged in vitro for the designated incubation times. To generate the soluble and insoluble fractions, the ‘hIAPP 24 h’ preparation was centrifuged at 21,000 \times g for 45 min and then the supernatant, which is the soluble fraction, was carefully removed and transferred to a 0.1 μ m spin filter tube. Next, the supernatant was filtered and the pelleted material, which is the insoluble fraction, was resuspended in the original total volume.

For the assays in **Figure 5** and **Figure 5—figure supplement 2**, 1 mM spine segment and 100 μ M full-length IAPP samples were generated by preparing the samples as described previously and then incubating them for 15 hr at room temperature under quiescent conditions. After the incubation period, the spine segments were diluted appropriately.

For all assays, 10 μ L of sample was added to cells. By doing this, samples were diluted 1/10 from in vitro stocks. Experiments were done in triplicate.

The appropriate statistical test for significance was determined by assessing whether (1) The sample sets had a Gaussian distribution using a D’Agostino-Pearson omnibus normality test and (2) The sample sets had equal variance using a Bartlett’s test or F test. For samples with Gaussian distributions and equal variances, we employed an unpaired t-test with equal standard deviations. For samples with Gaussian distributions, but unequal variances, we employed an unpaired t-test with Welch’s correction. For samples with non-Gaussian distributions and unequal variances, we employed a Mann-Whitney U-test.

3-(4,5-dimethylthiazol-2-yl)–2,5-diphenyltetrazolium bromide (MTT) dye reduction assay for cell viability

After a 24 hr incubation of samples with cells, 20 μ L of Thiazolyl Blue Tetrazolium Bromide MTT dye (Sigma, St. Louis, MO) was added to each well and incubated for 3.5 h at 37°C under sterile conditions. The MTT dye stock is 5 mg/mL in Dulbecco’s PBS. Next, the plate was removed from the incubator and 100 μ L of MTT stop solution (Cat. #4101, Promega, Madison, WI) was added to each well. We ensured the MTT crystals were fully dissolved by placing the plates on an orbital shaker (slow speed) for about an hour prior to taking measurements. Alternatively, the MTT assay was stopped by carefully aspirating off the culture media and adding 100 μ L of 100% DMSO to each well. Absorbance was measured at 570 nm using a SpectraMax M5. A background reading was recorded at 700 nm and subsequently subtracted from the 570 nm value.

Cells treated with vehicle alone (PBS + 0.1% DMSO) were designated at 100% viable, and cell viability of all other treatments was calculated accordingly.

For the MTT reduction assay in **Figure 6**, a single data point from the mIAPP sample set was deemed an outlier based on 2 lines of evidence: (1) The data point was identified as an outlier using a Grubb’s test ($\alpha = 0.1$) for outliers using the $n = 9$ sample set, and (2) When the sample set was pooled with more data collected for different experiments ($n = 42$), the data point was identified as an outlier using a more stringent Grubb’s test ($\alpha = 0.01$).

Caspase-3/7 activation assay

We used the caspase-3/7 GLO assay (Cat. # G8091, Promega, Madison, WI) to detect caspase-3/7 activation. For this assay, Rin5F cells were plated as previously described in white-walled 96-well plates (Cat. # 3917, Costar, Tewksbury, MA). After the designated aging period of each hIAPP preparation, 10 μ L of sample was added to cells and thus diluted 1/10 from in vitro stocks. Experiments were performed in triplicate. Samples were incubated with cells for 24 h. Next, cell culture media, caspase-3/7 reagent, and the cells were brought to room temperature. All media was aspirated from wells and then replaced with 25 μ L of media and 25 μ L of caspase-3/7 reagent and mixed thoroughly. The plate was incubated at room temperature for 30 min and then luminescence was

measured using a SpectraMax M5. Experimental points were normalized to vehicle-treated cells, which were designated as 100%. Cells treated with 2 μ M staurosporine were used as a positive control to ensure the assay kit worked correctly.

FRET-based real-time monitoring of caspase-3 activity

CHO cells were stably transfected with a vector producing EYFP and ECFP connected via a short linker containing the Asp-Glu-Val-Asp (DEVD) sequence targeted by activated caspase-3. The short linker allows fluorescence energy transfer (FRET) to occur between the two fluorophores. During apoptosis activated caspase-3 cleaves the linker resulting in a loss of FRET measured as a reduced 540 nm/480 nm emission ratio.

Cells were plated at 25,000 cells per well in black 96-well optical bottom plates (Nunc, Grand Island, NY) and the assay was performed in Krebs-Ringer (120 mM NaCl, 4.7 mM KCl, 2.5 mM CaCl_2 , 1.2 mM MgSO_4 , 0.5 mM KH_2PO_4 , pH 7.4) supplemented with 20 mM HEPES and 2 mM glucose (KRHG).

hAPP peptides (1–37, 15–25 WT and S20G, 19–29 WT and S20G) (final peptide concentration 50 μ M in 1% DMSO) were mixed with sonicated, preformed fibrils (seeds) made of the same peptide (corresponding to 166 nM of monomers) and immediately added to the plated cells. FRET was monitored in real-time by measuring emission at 480 nm and 540 nm with 440 nm excitation in a FLUOstar Omega microplate reader (BMG Labtech) over 24 hr at 37°C.

SDS sensitivity assay

Fibrils of 15–25 WT and 19–29 S20G at monomer equivalent concentrations were allowed to form for one week to ensure complete fibril formation. The samples were homogenized with vortexing, and then aliquoted to 0.5 mL tubes with equal volumes. Each fibril sample was treated with water or increasing amounts of SDS, and then heated at 55°C for 20 min. Next, an aliquot of each sample was transferred to a 384-well plate and turbidity was measured by recording absorbance at 340 nm. Each fibril sample was spotted onto a grid for negative-stain EM to analyze fibril abundance. The experiment was repeated twice, but the results of 1 experiment are shown in **Figure 4—figure supplement 1**.

Acknowledgements

We thank Dan Anderson for suggesting the use of FEM maps. We thank the Advanced Photon Source (APS) staff for beamline support during collection of fiber diffraction: M. Capel, K. Rajashankar, N. Sukumar, J. Schuermann, I. Kourinov and F. Murphy at NECAT beam lines 24-ID; the UCLA-DOE X-ray Crystallography Core Technology Center, Michael Collazo, and the UCLA-DOE Macromolecular Crystallization Core Technology Center for setting up initial crystallization screens; Ivo Atanasov and the Electron Imaging Center for NanoMachines (EICN) of California NanoSystems Institute (CNSI) at UCLA for the use of their electron microscopes; and the UCLA Statistical Consulting group for guidance on statistical computing. The UCLA-DOE X-ray and Macromolecular and Macromolecular Crystallization Core Technology Centers are supported in part by the Department of Energy grant DE-FC0302ER63421. Use of the Advanced Photon Source is supported by National Institutes of Health grants P41 RR015301 and P41 GM103403 and Department of Energy under Contract DE-AC02-06CH11357. We thank the Cure Alzheimer's Fund, the Swedish Research Council (VR 2015–02297), the Swedish Diabetes Foundation, the Janelia Research Campus visitor program, HHMI, and the National Institutes of Health (NIH) (R01 AG029430) for support.

Additional information

Funding

Funder	Grant reference number	Author
National Institutes of Health	R01 AG029430	Pascal Krotee Jose A Rodriguez Michael R Sawaya Duilio Cascio

Sarah Griner
David S Eisenberg

Howard Hughes Medical Institute

Pascal Krotee
Jose A Rodriguez
Michael R Sawaya
Duilio Cascio
Francis E Reyes
Dan Shi
Johan Hattne
Brent L Nannenga
Sarah Griner
Tamir Gonen
David S Eisenberg

Vetenskapsrådet VR 2015-02297

Marie E Oskarsson
Gunilla T Westermark

Swedish Diabetes Foundation

Marie E Oskarsson
Gunilla T Westermark

Cure Alzheimer's Fund

Stephan Philipp
Charles G Glabe

The funders had no role in study design, data collection and interpretation, or the decision to submit the work for publication.

Author contributions

PK, Conception and design, Acquisition of data, Analysis and interpretation of data, Drafting or revising the article, Contributed unpublished essential data or reagents; JAR, CGG, Acquisition of data, Analysis and interpretation of data, Contributed unpublished essential data or reagents; MRS, SP, Acquisition of data, Analysis and interpretation of data, Drafting or revising the article, Contributed unpublished essential data or reagents; DC, MEO, TG, Acquisition of data, Analysis and interpretation of data; FER, DS, JH, BLN, Acquired MicroED diffraction data, Acquisition of data; SG, Performed preliminary, unpublished dot blot assays for initial cytotoxicity studies; LJ, Conception and design, Analysis and interpretation of data; GTW, Suggested the FRET-based biosensor assay; Analyzed and interpreted FRET-based biosensor assay results; Helped compose responses to reviewers' comments, Analysis and interpretation of data; DSE, Conception and design, Analysis and interpretation of data, Drafting or revising the article

Author ORCIDs

Pascal Krotee, <http://orcid.org/0000-0002-9582-658X>

Michael R Sawaya, <http://orcid.org/0000-0003-0874-9043>

Duilio Cascio, <http://orcid.org/0000-0002-3877-6803>

Johan Hattne, <http://orcid.org/0000-0002-8936-0912>

Additional files

Supplementary files

- Supplementary file 1. Summary of structural features and biophysical properties of all hIAPP protein segment structures determined to date.

DOI: [10.7554/eLife.19273.024](https://doi.org/10.7554/eLife.19273.024)

References

- Abedini A**, Plesner A, Cao P, Ridgway Z, Zhang J, Tu LH, Middleton CT, Chao B, Sartori DJ, Meng F, Wang H, Wong AG, Zanni MT, Verchere CB, Raleigh DP, Schmidt AM, L-h T. 2016. Time-resolved studies define the nature of toxic IAPP intermediates, providing insight for anti-amyloidosis therapeutics. *eLife* **5**:e12977. doi: [10.7554/eLife.12977](https://doi.org/10.7554/eLife.12977), PMID: [27213520](https://pubmed.ncbi.nlm.nih.gov/27213520/)
- Afonine PV**, Moriarty NW, Mustyakimov M, Sobolev OV, Terwilliger TC, Turk D, Urzhumtsev A, Adams PD. 2015. FEM: feature-enhanced map. *Acta Crystallographica Section D Biological Crystallography* **71**:646–666. doi: [10.1107/S1399004714028132](https://doi.org/10.1107/S1399004714028132), PMID: [25760612](https://pubmed.ncbi.nlm.nih.gov/25760612/)

- Ashburn TT, Auger M, Lansbury PT. 1992. The structural basis of pancreatic amyloid formation: isotope-edited spectroscopy in the solid state. *Journal of the American Chemical Society* **114**:790–791. doi: [10.1021/ja00028a073](https://doi.org/10.1021/ja00028a073)
- Bedrood S, Li Y, Isas JM, Hegde BG, Baxa U, Haworth IS, Langen R. 2012. Fibril structure of human islet amyloid polypeptide. *The Journal of Biological Chemistry* **287**:5235–5241. doi: [10.1074/jbc.M111.327817](https://doi.org/10.1074/jbc.M111.327817), PMID: [22187437](https://pubmed.ncbi.nlm.nih.gov/22187437/)
- Bram Y, Frydman-Marom A, Yanai I, Gilead S, Shaltiel-Karyo R, Amdursky N, Gazit E. 2014. Apoptosis induced by islet amyloid polypeptide soluble oligomers is neutralized by diabetes-associated specific antibodies. *Scientific Reports* **4**:4267. doi: [10.1038/srep04267](https://doi.org/10.1038/srep04267), PMID: [24589570](https://pubmed.ncbi.nlm.nih.gov/24589570/)
- Budihardjo I, Oliver H, Lutter M, Luo X, Wang X. 1999. Biochemical pathways of caspase activation during apoptosis. *Annual Review of Cell and Developmental Biology* **15**:269–290. doi: [10.1146/annurev.cellbio.15.1.269](https://doi.org/10.1146/annurev.cellbio.15.1.269), PMID: [10611963](https://pubmed.ncbi.nlm.nih.gov/10611963/)
- Butler AE, Janson J, Bonner-Weir S, Ritzel R, Rizza RA, Butler PC. 2003. Beta-cell deficit and increased beta-cell apoptosis in humans with type 2 diabetes. *Diabetes* **52**:102–110. doi: [10.2337/diabetes.52.1.102](https://doi.org/10.2337/diabetes.52.1.102), PMID: [12502499](https://pubmed.ncbi.nlm.nih.gov/12502499/)
- Cao P, Tu LH, Abedini A, Levsh O, Akter R, Patsalo V, Schmidt AM, Raleigh DP. 2012. Sensitivity of amyloid formation by human islet amyloid polypeptide to mutations at residue 20. *Journal of Molecular Biology* **421**:282–295. doi: [10.1016/j.jmb.2011.12.032](https://doi.org/10.1016/j.jmb.2011.12.032), PMID: [22206987](https://pubmed.ncbi.nlm.nih.gov/22206987/)
- Chen VB, Arendall WB, Headd JJ, Keedy DA, Immormino RM, Kapral GJ, Murray LW, Richardson JS, Richardson DC. 2010. MolProbity: all-atom structure validation for macromolecular crystallography. *Acta Crystallographica Section D Biological Crystallography* **66**:12–21. doi: [10.1107/S0907444909042073](https://doi.org/10.1107/S0907444909042073)
- Collaborative Computational Project, Number 4. 1994. The CCP4 suite: programs for protein crystallography. *Acta Crystallographica. Section D, Biological Crystallography* **50**:760–763. doi: [10.1107/S0907444994003112](https://doi.org/10.1107/S0907444994003112), PMID: [15299374](https://pubmed.ncbi.nlm.nih.gov/15299374/)
- Colletier JP, Laganowsky A, Landau M, Zhao M, Soriaga AB, Goldschmidt L, Flot D, Cascio D, Sawaya MR, Eisenberg D. 2011. Molecular basis for amyloid-beta polymorphism. *PNAS* **108**:16938–16943. doi: [10.1073/pnas.1112600108](https://doi.org/10.1073/pnas.1112600108), PMID: [21949245](https://pubmed.ncbi.nlm.nih.gov/21949245/)
- Connolly ML. 1983. Solvent-accessible surfaces of proteins and nucleic acids. *Science* **221**:709–713. doi: [10.1126/science.6879170](https://doi.org/10.1126/science.6879170), PMID: [6879170](https://pubmed.ncbi.nlm.nih.gov/6879170/)
- Cooper GJ, Leighton B, Dimitriadis GD, Parry-Billings M, Kowalchuk JM, Howland K, Rothbard JB, Willis AC, Reid KB. 1988. Amylin found in amyloid deposits in human type 2 diabetes mellitus may be a hormone that regulates glycogen metabolism in skeletal muscle. *PNAS* **85**:7763–7766. doi: [10.1073/pnas.85.20.7763](https://doi.org/10.1073/pnas.85.20.7763), PMID: [3051005](https://pubmed.ncbi.nlm.nih.gov/3051005/)
- Cooper S, Khatib F, Treuille A, Barbero J, Lee J, Beenen M, Leaver-Fay A, Baker D, Popović Z, Players F. 2010. Predicting protein structures with a multiplayer online game. *Nature* **466**:756–760. doi: [10.1038/nature09304](https://doi.org/10.1038/nature09304), PMID: [20686574](https://pubmed.ncbi.nlm.nih.gov/20686574/)
- Diederichs K, Karplus PA. 2013. Better models by discarding data? *Acta Crystallographica Section D Biological Crystallography* **69**:1215–1222. doi: [10.1107/S0907444913001121](https://doi.org/10.1107/S0907444913001121)
- Eisenberg D, Jucker M. 2012. The amyloid state of proteins in human diseases. *Cell* **148**:1188–1203. doi: [10.1016/j.cell.2012.02.022](https://doi.org/10.1016/j.cell.2012.02.022), PMID: [22424229](https://pubmed.ncbi.nlm.nih.gov/22424229/)
- Eisenberg DS, Wesson M, Yamashita M. 1989. Interpretation of protein folding and binding with atomic solvation parameters. *Chemica Scripta* **29A**:217–221.
- Emsley P, Cowtan K. 2004. Coot: model-building tools for molecular graphics. *Acta Crystallographica. Section D, Biological Crystallography* **60**:2126–2132. doi: [10.1107/S0907444904019158](https://doi.org/10.1107/S0907444904019158), PMID: [15572765](https://pubmed.ncbi.nlm.nih.gov/15572765/)
- Esapa C, Moffitt JH, Novials A, McNamara CM, Levy JC, Laakso M, Gomis R, Clark A. 2005. Islet amyloid polypeptide gene promoter polymorphisms are not associated with type 2 diabetes or with the severity of islet amyloidosis. *Biochimica Et Biophysica Acta* **1740**:74–78. doi: [10.1016/j.bbadis.2005.02.001](https://doi.org/10.1016/j.bbadis.2005.02.001), PMID: [15878744](https://pubmed.ncbi.nlm.nih.gov/15878744/)
- Gazdar AF, Chick WL, Oie HK, Sims HL, King DL, Weir GC, Lauris V. 1980. Continuous, clonal, insulin- and somatostatin-secreting cell lines established from a transplantable rat islet cell tumor. *PNAS* **77**:3519–3523. doi: [10.1073/pnas.77.6.3519](https://doi.org/10.1073/pnas.77.6.3519), PMID: [6106192](https://pubmed.ncbi.nlm.nih.gov/6106192/)
- Goldsbury C, Goldie K, Pellaud J, Seelig J, Frey P, Müller SA, Kistler J, Cooper GJ, Aepli U. 2000. Amyloid fibril formation from full-length and fragments of amylin. *Journal of Structural Biology* **130**:352–362. doi: [10.1006/jsbi.2000.4268](https://doi.org/10.1006/jsbi.2000.4268), PMID: [10940238](https://pubmed.ncbi.nlm.nih.gov/10940238/)
- Goldsbury CS, Cooper GJ, Goldie KN, Müller SA, Saafi EL, Gruijters WT, Misur MP, Engel A, Aepli U, Kistler J. 1997. Polymorphic fibrillar assembly of human amylin. *Journal of Structural Biology* **119**:17–27. doi: [10.1006/jsbi.1997.3858](https://doi.org/10.1006/jsbi.1997.3858), PMID: [9216085](https://pubmed.ncbi.nlm.nih.gov/9216085/)
- Griffiths JM, Ashburn TT, Auger M, Costa PR, Griffin RG, Lansbury PT. 1995. Rotational resonance solid-state NMR elucidates a structural model of pancreatic amyloid. *Journal of the American Chemical Society* **117**:3539–3546. doi: [10.1021/ja00117a023](https://doi.org/10.1021/ja00117a023)
- Haataja L, Gurlo T, Huang CJ, Butler PC. 2008. Islet amyloid in type 2 diabetes, and the toxic oligomer hypothesis. *Endocrine Reviews* **29**:303–316. doi: [10.1210/er.2007-0037](https://doi.org/10.1210/er.2007-0037), PMID: [18314421](https://pubmed.ncbi.nlm.nih.gov/18314421/)
- Hattne J, Reyes FE, Nannenga BL, Shi D, de la Cruz MJ, Leslie AGW, Gonen T. 2015. MicroED data collection and processing. *Acta Crystallographica Section A Foundations and Advances* **71**:353–360. doi: [10.1107/S2053273315010669](https://doi.org/10.1107/S2053273315010669)
- Hiddinga HJ, Eberhardt NL. 1999. Intracellular amyloidogenesis by human islet amyloid polypeptide induces apoptosis in COS-1 cells. *The American Journal of Pathology* **154**:1077–1088. doi: [10.1016/S0002-9440\(10\)65360-6](https://doi.org/10.1016/S0002-9440(10)65360-6), PMID: [10233846](https://pubmed.ncbi.nlm.nih.gov/10233846/)

- Huang CJ, Lin CY, Haataja L, Gurlo T, Butler AE, Rizza RA, Butler PC. 2007. High expression rates of human islet amyloid polypeptide induce endoplasmic reticulum stress mediated beta-cell apoptosis, a characteristic of humans with type 2 but not type 1 diabetes. *Diabetes* **56**:2016–2027. doi: [10.2337/db07-0197](https://doi.org/10.2337/db07-0197), PMID: 17475933
- Hull RL, Shen ZP, Watts MR, Kodama K, Carr DB, Utzschneider KM, Zraika S, Wang F, Kahn SE. 2005b. Long-term treatment with rosiglitazone and metformin reduces the extent of, but does not prevent, islet amyloid deposition in mice expressing the gene for human islet amyloid polypeptide. *Diabetes* **54**:2235–2244. doi: [10.2337/diabetes.54.7.2235](https://doi.org/10.2337/diabetes.54.7.2235), PMID: 15983227
- Hull RL, Watts MR, Kodama K, Shen Z, Utzschneider KM, Carr DB, Vidal J, Kahn SE. 2005a. Genetic background determines the extent of islet amyloid formation in human islet amyloid polypeptide transgenic mice. *AJP: Endocrinology and Metabolism* **289**:E703–E709. doi: [10.1152/ajpendo.00471.2004](https://doi.org/10.1152/ajpendo.00471.2004)
- Höppner JW, Åhrén B, Lips CJ. 2000. Islet amyloid and type 2 diabetes mellitus. *The New England Journal of Medicine* **343**:411–419. doi: [10.1056/NEJM200008103430607](https://doi.org/10.1056/NEJM200008103430607), PMID: 10933741
- Ivanova MI, Sievers SA, Sawaya MR, Wall JS, Eisenberg D. 2009. Molecular basis for insulin fibril assembly. *PNAS* **106**:18990–18995. doi: [10.1073/pnas.0910080106](https://doi.org/10.1073/pnas.0910080106), PMID: 19864624
- Jack E, Newsome M, Stockley PG, Radford SE, Middleton DA. 2006. The organization of aromatic side groups in an amyloid fibril probed by solid-state ²H and ¹⁹F NMR spectroscopy. *Journal of the American Chemical Society* **128**:8098–8099. doi: [10.1021/ja0581898](https://doi.org/10.1021/ja0581898), PMID: 16787049
- Janson J, Soeller WC, Roche PC, Nelson RT, Torchia AJ, Kreutter DK, Butler PC. 1996. Spontaneous diabetes mellitus in transgenic mice expressing human islet amyloid polypeptide. *PNAS* **93**:7283–7288. doi: [10.1073/pnas.93.14.7283](https://doi.org/10.1073/pnas.93.14.7283), PMID: 8692984
- Jurgens CA, Toukatly MN, Fligner CL, Udayasankar J, Subramanian SL, Zraika S, Aston-Mourney K, Carr DB, Westermark P, Westermark GT, Kahn SE, Hull RL. 2011. β -cell loss and β -cell apoptosis in human type 2 diabetes are related to islet amyloid deposition. *The American Journal of Pathology* **178**:2632–2640. doi: [10.1016/j.ajpath.2011.02.036](https://doi.org/10.1016/j.ajpath.2011.02.036), PMID: 21641386
- Kabsch W. 2010. XDS. *Acta Crystallographica. Section D, Biological Crystallography* **66**:125–132. doi: [10.1107/S0907444909047337](https://doi.org/10.1107/S0907444909047337), PMID: 20124692
- Kahn SE, Cooper ME, Del Prato S. 2014. Pathophysiology and treatment of type 2 diabetes: perspectives on the past, present, and future. *Lancet* **383**:1068–1083. doi: [10.1016/S0140-6736\(13\)62154-6](https://doi.org/10.1016/S0140-6736(13)62154-6), PMID: 24315620
- Kajava AV, Aebi U, Steven AC. 2005. The parallel superpleated beta-structure as a model for amyloid fibrils of human amylin. *Journal of Molecular Biology* **348**:247–252. doi: [10.1016/j.jmb.2005.02.029](https://doi.org/10.1016/j.jmb.2005.02.029), PMID: 15811365
- Kapurniotu A. 2001. Amyloidogenicity and cytotoxicity of islet amyloid polypeptide. *Biopolymers* **60**:438–459. doi: [10.1002/1097-0282\(2001\)60:6<438::AID-BIP10182>3.0.CO;2-A](https://doi.org/10.1002/1097-0282(2001)60:6<438::AID-BIP10182>3.0.CO;2-A)
- Kayed R, Head E, Sarsoza F, Saing T, Cotman CW, Necula M, Margol L, Wu J, Breydo L, Thompson JL, Rasool S, Gurlo T, Butler P, Glabe CG. 2007. Fibril specific, conformation dependent antibodies recognize a generic epitope common to amyloid fibrils and fibrillar oligomers that is absent in prefibrillar oligomers. *Molecular Neurodegeneration* **2**:18. doi: [10.1186/1750-1326-2-18](https://doi.org/10.1186/1750-1326-2-18), PMID: 17897471
- Kyte J, Doolittle RF. 1982. A simple method for displaying the hydropathic character of a protein. *Journal of Molecular Biology* **157**:105–132. doi: [10.1016/0022-2836\(82\)90515-0](https://doi.org/10.1016/0022-2836(82)90515-0), PMID: 7108955
- Laganowsky A, Liu C, Sawaya MR, Whitelegge JP, Park J, Zhao M, Pensalfini A, Soriaga AB, Landau M, Teng PK, Cascio D, Glabe C, Eisenberg D. 2012. Atomic view of a toxic amyloid small oligomer. *Science* **335**:1228–1231. doi: [10.1126/science.1213151](https://doi.org/10.1126/science.1213151), PMID: 22403391
- Lawrence MC, Colman PM. 1993. Shape complementarity at protein/protein interfaces. *Journal of Molecular Biology* **234**:946–950. doi: [10.1006/jmbi.1993.1648](https://doi.org/10.1006/jmbi.1993.1648), PMID: 8263940
- Lee B, Richards FM. 1971. The interpretation of protein structures: estimation of static accessibility. *Journal of Molecular Biology* **55**:379–400. doi: [10.1016/0022-2836\(71\)90324-X](https://doi.org/10.1016/0022-2836(71)90324-X), PMID: 5551392
- Lee SC, Hashim Y, Li JK, Ko GT, Critchley JA, Cockram CS, Chan JC. 2001. The islet amyloid polypeptide (amylin) gene S20G mutation in Chinese subjects: evidence for associations with type 2 diabetes and cholesterol levels. *Clinical Endocrinology* **54**:541–546. doi: [10.1046/j.1365-2265.2001.01244.x](https://doi.org/10.1046/j.1365-2265.2001.01244.x), PMID: 11318791
- Lin CY, Gurlo T, Kayed R, Butler AE, Haataja L, Glabe CG, Butler PC. 2007. Toxic human islet amyloid polypeptide (h-IAPP) oligomers are intracellular, and vaccination to induce anti-toxic oligomer antibodies does not prevent h-IAPP-induced beta-cell apoptosis in h-IAPP transgenic mice. *Diabetes* **56**:1324–1332. doi: [10.2337/db06-1579](https://doi.org/10.2337/db06-1579), PMID: 17353506
- Liu C, Sawaya MR, Eisenberg D. 2011. β_2 -microglobulin forms three-dimensional domain-swapped amyloid fibrils with disulfide linkages. *Nature structural & molecular biology* **18**:49–55. doi: [10.1038/nsmb.1948](https://doi.org/10.1038/nsmb.1948), PMID: 21131979
- Liu C, Zhao M, Jiang L, Cheng PN, Park J, Sawaya MR, Pensalfini A, Gou D, Berk AJ, Glabe CG, Nowick J, Eisenberg D. 2012. Out-of-register β -sheets suggest a pathway to toxic amyloid aggregates. *PNAS* **109**:20913–20918. doi: [10.1073/pnas.1218792109](https://doi.org/10.1073/pnas.1218792109), PMID: 23213214
- Liu S, Hattne J, Reyes FE, Sanchez-Martinez S, Jason de la Cruz M, Shi D, Gonen T. 2016. Atomic resolution structure determination by the cryo-EM method MicroED. *Protein Science : A Publication of the Protein Society* **00**:1–8. doi: [10.1002/pro.2989](https://doi.org/10.1002/pro.2989)
- Liu Y, Peterson DA, Kimura H, Schubert D. 1997. Mechanism of cellular 3-(4,5-dimethylthiazol-2-yl)-2,5-diphenyltetrazolium bromide (MTT) reduction. *Journal of Neurochemistry* **69**:581–593. doi: [10.1046/j.1471-4159.1997.69020581.x](https://doi.org/10.1046/j.1471-4159.1997.69020581.x)

- Liu Y, Schubert D. 1997. Cytotoxic amyloid peptides inhibit cellular 3-(4,5-dimethylthiazol-2-yl)-2,5-diphenyltetrazolium bromide (MTT) reduction by enhancing MTT formazan exocytosis. *Journal of Neurochemistry* **69**:2285–2293. doi: [10.1046/j.1471-4159.1997.69062285.x](https://doi.org/10.1046/j.1471-4159.1997.69062285.x), PMID: 9375659
- Lorenzo A, Razzaboni B, Weir GC, Yankner BA. 1994. Pancreatic islet cell toxicity of Amylin associated with type-2 diabetes mellitus. *Nature* **368**:756–760. doi: [10.1038/368756a0](https://doi.org/10.1038/368756a0), PMID: 8152488
- Lorenzo A, Yankner BA. 1994. Beta-amyloid neurotoxicity requires fibril formation and is inhibited by congo red. *PNAS* **91**:12243–12247. doi: [10.1073/pnas.91.25.12243](https://doi.org/10.1073/pnas.91.25.12243), PMID: 7991613
- Luca S, Yau WM, Leapman R, Tycko R. 2007. Peptide conformation and supramolecular organization in amylin fibrils: constraints from solid-state NMR. *Biochemistry* **46**:13505–13522. doi: [10.1021/bi701427q](https://doi.org/10.1021/bi701427q), PMID: 17979302
- Madine J, Jack E, Stockley PG, Radford SE, Serpell LC, Middleton DA. 2008. Structural insights into the polymorphism of amyloid-like fibrils formed by region 20–29 of Amylin revealed by solid-state NMR and X-ray fiber diffraction. *Journal of the American Chemical Society* **130**:14990–15001. doi: [10.1021/ja802483d](https://doi.org/10.1021/ja802483d), PMID: 18937465
- Magzoub M, Miranker AD. 2012. Concentration-dependent transitions govern the subcellular localization of islet amyloid polypeptide. *FASEB Journal : Official Publication of the Federation of American Societies for Experimental Biology* **26**:1228–1238. doi: [10.1096/fj.11-194613](https://doi.org/10.1096/fj.11-194613), PMID: 22183778
- Maloy AL, Longnecker DS, Greenberg ER. 1981. The relation of islet amyloid to the clinical type of diabetes. *Human Pathology* **12**:917–922. doi: [10.1016/S0046-8177\(81\)80197-9](https://doi.org/10.1016/S0046-8177(81)80197-9), PMID: 7028600
- McCoy AJ, Grosse-Kunstleve RW, Storoni LC, Read RJ. 2005. Likelihood-enhanced fast translation functions. *Acta Crystallographica Section D Biological Crystallography* **61**:458–464. doi: [10.1107/S0907444905001617](https://doi.org/10.1107/S0907444905001617), PMID: 15805601
- McCoy AJ. 2007. Solving structures of protein complexes by molecular replacement with phaser. *Acta Crystallographica. Section D, Biological Crystallography* **63**:32–41. doi: [10.1107/S0907444906045975](https://doi.org/10.1107/S0907444906045975), PMID: 17164524
- Meier DT, Entrup L, Templin AT, Hogan MF, Mellati M, Zraika S, Hull RL, Kahn SE. 2016. The S20G substitution in hIAPP is more amyloidogenic and cytotoxic than wild-type hIAPP in mouse islets. *Diabetologia* **59**:2166–2171. doi: [10.1007/s00125-016-4045-x](https://doi.org/10.1007/s00125-016-4045-x), PMID: 27393137
- Meier JJ, Kayed R, Lin C-Y, Gurlo T, Haataja L, Jayasinghe S, Langen R, Glabe CG, Butler PC. 2006. Inhibition of human IAPP fibril formation does not prevent beta-cell death: evidence for distinct actions of oligomers and fibrils of human IAPP. *AJP: Endocrinology and Metabolism* **291**:E1317–E1324. doi: [10.1152/ajpendo.00082.2006](https://doi.org/10.1152/ajpendo.00082.2006)
- Meng F, Abedini A, Plesner A, Verchere CB, Raleigh DP. 2010. The flavanol (-)-epigallocatechin 3-gallate inhibits amyloid formation by islet amyloid polypeptide, disaggregates amyloid fibrils, and protects cultured cells against IAPP-induced toxicity. *Biochemistry* **49**:8127–8133. doi: [10.1021/bi100939a](https://doi.org/10.1021/bi100939a), PMID: 20707388
- Mirecka EA, Feuerstein S, Gremer L, Schröder GF, Stoldt M, Willbold D, Hoyer W. 2016. β -hairpin of islet amyloid polypeptide bound to an aggregation inhibitor. *Scientific Reports* **6**:33474. doi: [10.1038/srep33474](https://doi.org/10.1038/srep33474)
- Moriarty DF, Raleigh DP. 1999. Effects of sequential proline substitutions on amyloid formation by human amylin20–29. *Biochemistry* **38**:1811–1818. doi: [10.1021/bi981658g](https://doi.org/10.1021/bi981658g), PMID: 10026261
- Morita S, Sakagashira S, Ueyama M, Shimajiri Y, Furuta M, Sanke T. 2011. Progressive deterioration of insulin secretion in Japanese type 2 diabetic patients in comparison with those who carry the S20G mutation of the islet amyloid polypeptide gene: A long-term follow-up study. *Journal of Diabetes Investigation* **2**:287–292. doi: [10.1111/j.2040-1124.2011.00102.x](https://doi.org/10.1111/j.2040-1124.2011.00102.x), PMID: 24843500
- Mosmann T. 1983. Rapid colorimetric assay for cellular growth and survival: application to proliferation and cytotoxicity assays. *Journal of Immunological Methods* **65**:55–63. doi: [10.1016/0022-1759\(83\)90303-4](https://doi.org/10.1016/0022-1759(83)90303-4), PMID: 6606682
- Mukherjee A, Morales-Scheihing D, Butler PC, Soto C. 2015. Type 2 diabetes as a protein misfolding disease. *Trends in Molecular Medicine* **21**:439–449. doi: [10.1016/j.molmed.2015.04.005](https://doi.org/10.1016/j.molmed.2015.04.005), PMID: 25998900
- Mulder H, Ling C. 2009. Mitochondrial dysfunction in pancreatic beta-cells in type 2 diabetes. *Molecular and Cellular Endocrinology* **297**:34–40. doi: [10.1016/j.mce.2008.05.015](https://doi.org/10.1016/j.mce.2008.05.015), PMID: 18606489
- Nannenga BL, Shi D, Hattne J, Reyes FE, Gonen T. 2014a. Structure of catalase determined by MicroED. *eLife* **3**:e03600. doi: [10.7554/eLife.03600](https://doi.org/10.7554/eLife.03600), PMID: 25303172
- Nannenga BL, Shi D, Leslie AG, Gonen T. 2014b. High-resolution structure determination by continuous-rotation data collection in MicroED. *Nature Methods* **11**:1–5. doi: [10.1038/nmeth.3043](https://doi.org/10.1038/nmeth.3043), PMID: 25086503
- Nelson R, Sawaya MR, Balbirnie M, Madsen AØ, Riekel C, Grothe R, Eisenberg D. 2005. Structure of the cross-beta spine of amyloid-like fibrils. *Nature* **435**:773–778. doi: [10.1038/nature03680](https://doi.org/10.1038/nature03680), PMID: 15944695
- Nielsen JT, Bjerring M, Jeppesen MD, Pedersen RO, Pedersen JM, Hein KL, Vosegaard T, Skrydstrup T, Otzen DE, Nielsen NC. 2009. Unique identification of supramolecular structures in amyloid fibrils by solid-state NMR spectroscopy. *Angewandte Chemie International Edition* **48**:2118–2121. doi: [10.1002/anie.200804198](https://doi.org/10.1002/anie.200804198)
- Nishi M, Chan SJ, Nagamatsu S, Bell GI, Steiner DF. 1989. Conservation of the sequence of islet amyloid polypeptide in five mammals is consistent with its putative role as an islet hormone. *PNAS* **86**:5738–5742. doi: [10.1073/pnas.86.15.5738](https://doi.org/10.1073/pnas.86.15.5738), PMID: 2668946
- O'Brien TD, Butler PC, Kreutter DK, Kane LA, Eberhardt NL. 1995. Human islet amyloid polypeptide expression in COS-1 cells. A model of intracellular amyloidogenesis. *The American Journal of Pathology* **147**:609–616. PMID: 7677175
- Opie EL. 1901. The relation of diabetes mellitus to lesions of the pancreas. hyaline degeneration of the islands of Langerhans. *Journal of Experimental Medicine* **5**:527–541. doi: [10.1084/jem.5.5.527](https://doi.org/10.1084/jem.5.5.527), PMID: 19866956

- Oskarsson ME**, Singh K, Wang J, Vlodavsky I, Li JP, Westermark GT. 2015. Heparan sulfate proteoglycans are important for islet amyloid formation and islet amyloid Polypeptide-induced apoptosis. *The Journal of Biological Chemistry* **290**:15121–15132. doi: [10.1074/jbc.M114.631697](https://doi.org/10.1074/jbc.M114.631697), PMID: [25922077](https://pubmed.ncbi.nlm.nih.gov/25922077/)
- Paulsson JF**, Schultz SW, Köhler M, Leibiger I, Berggren P-O, Westermark GT. 2008. Real-time monitoring of apoptosis by caspase-3-like protease induced FRET reduction triggered by amyloid aggregation. *Experimental Diabetes Research* **2008**:1–12. doi: [10.1155/2008/865850](https://doi.org/10.1155/2008/865850)
- Pilkington EH**, Gurzov EN, Kallinen A, Litwak SA, Stanley WJ, Davis TP, Ke PC. 2016. Pancreatic β -Cell membrane fluidity and toxicity induced by human islet amyloid polypeptide species. *Scientific Reports* **6**:21274. doi: [10.1038/srep21274](https://doi.org/10.1038/srep21274), PMID: [26880502](https://pubmed.ncbi.nlm.nih.gov/26880502/)
- Richards FM**. 1977. Areas, volumes, packing, and protein structure. *Annual Review of Biophysics and Bioengineering* **6**:151–176. doi: [10.1146/annurev.bb.06.060177.001055](https://doi.org/10.1146/annurev.bb.06.060177.001055)
- Ritzel RA**, Meier JJ, Lin CY, Veldhuis JD, Butler PC. 2007. Human islet amyloid polypeptide oligomers disrupt cell coupling, induce apoptosis, and impair insulin secretion in isolated human islets. *Diabetes* **56**:65–71. doi: [10.2337/db06-0734](https://doi.org/10.2337/db06-0734), PMID: [17192466](https://pubmed.ncbi.nlm.nih.gov/17192466/)
- Roberts AN**, Leighton B, Todd JA, Cockburn D, Schofield PN, Sutton R, Holt S, Boyd Y, Day AJ, Foot EA. 1989. Molecular and functional characterization of amylin, a peptide associated with type 2 diabetes mellitus. *PNAS* **86**:9662–9666. doi: [10.1073/pnas.86.24.9662](https://doi.org/10.1073/pnas.86.24.9662), PMID: [2690069](https://pubmed.ncbi.nlm.nih.gov/2690069/)
- Rodriguez JA**, Ivanova MI, Sawaya MR, Cascio D, Reyes FE, Shi D, Sangwan S, Guenther EL, Johnson LM, Zhang M, Jiang L, Arbing MA, Nannenga BL, Hattne J, Whitelegge J, Brewster AS, Messerschmidt M, Boutet S, Sauter NK, Gonen T, et al. 2015. Structure of the toxic core of α -synuclein from invisible crystals. *Nature* **525**:486–490. doi: [10.1038/nature15368](https://doi.org/10.1038/nature15368), PMID: [26352473](https://pubmed.ncbi.nlm.nih.gov/26352473/)
- Sakagashira S**, Hiddinga HJ, Tateishi K, Sanke T, Hanabusa T, Nanjo K, Eberhardt NL. 2000. S20G mutant Amylin exhibits increased in vitro amyloidogenicity and increased intracellular cytotoxicity compared to wild-type Amylin. *The American Journal of Pathology* **157**:2101–2109. doi: [10.1016/S0002-9440\(10\)64848-1](https://doi.org/10.1016/S0002-9440(10)64848-1), PMID: [11106582](https://pubmed.ncbi.nlm.nih.gov/11106582/)
- Sakagashira S**, Sanke T, Hanabusa T, Shimomura H, Ohagi S, Kumagaye KY, Nakajima K, Nanjo K. 1996. Missense mutation of amylin gene (S20G) in Japanese NIDDM patients. *Diabetes* **45**:1279–1281. doi: [10.2337/diab.45.9.1279](https://doi.org/10.2337/diab.45.9.1279), PMID: [8772735](https://pubmed.ncbi.nlm.nih.gov/8772735/)
- Sawaya MR**, Sambashivan S, Nelson R, Ivanova MI, Sievers SA, Apostol MI, Thompson MJ, Balbirnie M, Wiltzius JJ, McFarlane HT, Madsen AØ, Riekel C, Eisenberg D. 2007. Atomic structures of amyloid cross-beta spines reveal varied steric zippers. *Nature* **447**:453–457. doi: [10.1038/nature05695](https://doi.org/10.1038/nature05695), PMID: [17468747](https://pubmed.ncbi.nlm.nih.gov/17468747/)
- Schlamadinger DE**, Miranker AD. 2014. Fiber-dependent and -independent toxicity of islet amyloid polypeptide. *Biophysical Journal* **107**:2559–2566. doi: [10.1016/j.bpj.2014.09.047](https://doi.org/10.1016/j.bpj.2014.09.047), PMID: [25468335](https://pubmed.ncbi.nlm.nih.gov/25468335/)
- Schubert D**, Behl C, Lesley R, Brack A, Dargusch R, Sagara Y, Kimura H. 1995. Amyloid peptides are toxic via a common oxidative mechanism. *PNAS* **92**:1989–1993. doi: [10.1073/pnas.92.6.1989](https://doi.org/10.1073/pnas.92.6.1989), PMID: [7892213](https://pubmed.ncbi.nlm.nih.gov/7892213/)
- Sevigny J**, Chiao P, Bussière T, Weinreb PH, Williams L, Maier M, Dunstan R, Salloway S, Chen T, Ling Y, O’Gorman J, Qian F, Arastu M, Li M, Chollate S, Brennan MS, Quintero-Monzon O, Scannevin RH, Arnold HM, Engber T, et al. 2016. The antibody aducanumab reduces $A\beta$ plaques in Alzheimer’s disease. *Nature* **537**:50–56. doi: [10.1038/nature19323](https://doi.org/10.1038/nature19323), PMID: [27582220](https://pubmed.ncbi.nlm.nih.gov/27582220/)
- Shi D**, Nannenga BL, de la Cruz MJ, Liu J, Sawtelle S, Calero G, Reyes FE, Hattne J, Gonen T. 2016. The collection of MicroED data for macromolecular crystallography. *Nature Protocols* **11**:895–904. doi: [10.1038/nprot.2016.046](https://doi.org/10.1038/nprot.2016.046), PMID: [27077331](https://pubmed.ncbi.nlm.nih.gov/27077331/)
- Shi D**, Nannenga BL, Iadanza MG, Gonen T. 2013. Three-dimensional electron crystallography of protein microcrystals. *eLife* **2**:e01345. doi: [10.7554/eLife.01345](https://doi.org/10.7554/eLife.01345), PMID: [24252878](https://pubmed.ncbi.nlm.nih.gov/24252878/)
- Sievers SA**, Karanicolas J, Chang HW, Zhao A, Jiang L, Zirafi O, Stevens JT, Münch J, Baker D, Eisenberg D. 2011. Structure-based design of non-natural amino-acid inhibitors of amyloid fibril formation. *Nature* **475**:96–100. doi: [10.1038/nature10154](https://doi.org/10.1038/nature10154), PMID: [21677644](https://pubmed.ncbi.nlm.nih.gov/21677644/)
- Soriaga AB**, Sangwan S, Macdonald R, Sawaya MR, Eisenberg D. 2016. Crystal structures of IAPP amyloidogenic segments reveal a novel packing motif of out-of-register beta sheets. *The Journal of Physical Chemistry B* **120**:5810–5816. doi: [10.1021/acs.jpcc.5b09981](https://doi.org/10.1021/acs.jpcc.5b09981)
- Sunde M**, Serpell LC, Bartlam M, Fraser PE, Pepys MB, Blake CC. 1997. Common core structure of amyloid fibrils by synchrotron X-ray diffraction. *Journal of Molecular Biology* **273**:729–739. doi: [10.1006/jmbi.1997.1348](https://doi.org/10.1006/jmbi.1997.1348), PMID: [9356260](https://pubmed.ncbi.nlm.nih.gov/9356260/)
- Tenidis K**, Waldner M, Bernhagen J, Fischle W, Bergmann M, Weber M, Merkle ML, Voelter W, Brunner H, Kapurniotu A. 2000. Identification of a Penta- and hexapeptide of islet amyloid polypeptide (IAPP) with amyloidogenic and cytotoxic properties. *Journal of Molecular Biology* **295**:1055–1071. doi: [10.1006/jmbi.1999.3422](https://doi.org/10.1006/jmbi.1999.3422), PMID: [10656810](https://pubmed.ncbi.nlm.nih.gov/10656810/)
- Tomasello MF**, Sinopoli A, Attanasio F, Giuffrida ML, Campagna T, Milardi D, Pappalardo G. 2014. Molecular and cytotoxic properties of hIAPP17-29 and rIAPP17-29 fragments: a comparative study with the respective full-length parent polypeptides. *European Journal of Medicinal Chemistry* **81**:442–455. doi: [10.1016/j.ejmech.2014.05.038](https://doi.org/10.1016/j.ejmech.2014.05.038), PMID: [24859763](https://pubmed.ncbi.nlm.nih.gov/24859763/)
- Verchere CB**, D’Alessio DA, Palmiter RD, Weir GC, Bonner-Weir S, Baskin DG, Kahn SE. 1996. Islet amyloid formation associated with hyperglycemia in transgenic mice with pancreatic beta cell expression of human islet amyloid polypeptide. *PNAS* **93**:3492–3496. doi: [10.1073/pnas.93.8.3492](https://doi.org/10.1073/pnas.93.8.3492), PMID: [8622964](https://pubmed.ncbi.nlm.nih.gov/8622964/)
- Weirich F**, Gremer L, Mirecka EA, Schiefer S, Hoyer W, Heise H. 2016. Structural characterization of fibrils from recombinant human islet amyloid polypeptide by Solid-State NMR: The central FGAILS segment is part of the β -Sheet core. *PLoS One* **11**:e0161243. doi: [10.1371/journal.pone.0161243](https://doi.org/10.1371/journal.pone.0161243), PMID: [27607147](https://pubmed.ncbi.nlm.nih.gov/27607147/)

- Westermarck GT**, Gebre-Medhin S, Steiner DF, Westermarck P. 2000. Islet amyloid development in a mouse strain lacking endogenous islet amyloid polypeptide (IAPP) but expressing human IAPP. *Molecular Medicine* **6**:998–1007. PMID: 11474116
- Westermarck P**, Andersson A, Westermarck GT. 2011. Islet amyloid polypeptide, islet amyloid, and diabetes mellitus. *Physiological Reviews* **91**:795–826. doi: 10.1152/physrev.00042.2009, PMID: 21742788
- Westermarck P**, Engström U, Johnson KH, Westermarck GT, Betsholtz C. 1990. Islet amyloid polypeptide: pinpointing amino acid residues linked to amyloid fibril formation. *PNAS* **87**:5036–5040. doi: 10.1073/pnas.87.13.5036, PMID: 2195544
- Westermarck P**, Wernstedt C, Wilander E, Hayden DW, O'Brien TD, Johnson KH. 1987. Amyloid fibrils in human insulinoma and islets of Langerhans of the diabetic cat are derived from a neuropeptide-like protein also present in normal islet cells. *PNAS* **84**:3881–3885. doi: 10.1073/pnas.84.11.3881, PMID: 3035556
- Wiltzius JJ**, Landau M, Nelson R, Sawaya MR, Apostol MI, Goldschmidt L, Soriaga AB, Cascio D, Rajashankar K, Eisenberg D. 2009a. Molecular mechanisms for protein-encoded inheritance. *Nature Structural & Molecular Biology* **16**:973–978. doi: 10.1038/nsmb.1643, PMID: 19684598
- Wiltzius JJ**, Sievers SA, Sawaya MR, Cascio D, Popov D, Riek C, Eisenberg D. 2008. Atomic structure of the cross-beta spine of islet amyloid polypeptide (amylin). *Protein Science : A Publication of the Protein Society* **17**:1467–1474. doi: 10.1110/ps.036509.108, PMID: 18556473
- Wiltzius JJ**, Sievers SA, Sawaya MR, Eisenberg D. 2009b. Atomic structures of IAPP (amylin) fusions suggest a mechanism for fibrillation and the role of insulin in the process. *Protein Science : A Publication of the Protein Society* **18**:1521–1530. doi: 10.1002/pro.145, PMID: 19475663
- Wineman-Fisher V**, Atsmon-Raz Y, Miller Y. 2015. Orientations of residues along the β -arch of self-assembled Amylin fibril-like structures lead to polymorphism. *Biomacromolecules* **16**:156–165. doi: 10.1021/bm501326y, PMID: 25420121
- Wu JW**, Breydo L, Isas JM, Lee J, Kuznetsov YG, Langen R, Glabe C. 2010. Fibrillar oligomers nucleate the oligomerization of monomeric amyloid beta but do not seed fibril formation. *The Journal of Biological Chemistry* **285**:6071–6079. doi: 10.1074/jbc.M109.069542, PMID: 20018889
- Young LM**, Saunders JC, Mahood RA, Revell CH, Foster RJ, Tu LH, Raleigh DP, Radford SE, Ashcroft AE. 2015. Screening and classifying small-molecule inhibitors of amyloid formation using ion mobility spectrometry-mass spectrometry. *Nature Chemistry* **7**:73–81. doi: 10.1038/nchem.2129, PMID: 25515893
- Yu L**, Lee SJ, Yee VC. 2015. Crystal structures of polymorphic prion protein β 1 peptides reveal variable steric zipper conformations. *Biochemistry* **54**:3640–3648. doi: 10.1021/acs.biochem.5b00425, PMID: 25978088
- Zraika S**, Hull RL, Verchere CB, Clark A, Potter KJ, Fraser PE, Raleigh DP, Kahn SE. 2010. Toxic oligomers and islet beta cell death: guilty by association or convicted by circumstantial evidence? *Diabetologia* **53**:1046–1056. doi: 10.1007/s00125-010-1671-6, PMID: 20182863